UNIVERSITY OF OKLAHOMA

GRADUATE COLLEGE

INVESTIGATION OF LOW-POWER ANTENNA RECONFIGURATION THROUGH BIASING OF MAGNETIC LOADS

A THESIS

SUBMITTED TO THE GRADUATE FACULTY

in partial fulfillment of the requirements for the

Degree of

MASTER OF SCIENCE

By

ADAM HORTON
Norman, Oklahoma
2017

INVESTIGATION OF LOW-POWER ANTENNA RECONFIGURATION
THROUGH BIASING OF MAGNETIC LOADS

A THESIS APPROVED FOR THE
SCHOOL OF ELECTRICAL AND COMPUTER ENGINEERING

BY

Dr. Jessica Ruyle, Chair

Dr. Caleb Fulton

Dr. Hjalti Sigmarsson

Table of Contents

List of Figures

Abstract

In modern RF systems, tunable devices are increasingly necessary to provide agility in crowded spectral environments. The antenna, as an integral part of any wireless system, must be capable of operating well at multiple frequencies and in a variety of environments where space and spectrum are at a premium. This work presents a novel method of magnetic reconfiguration through actuation of a ferrofluid load with a permanent magnetic field. When compared with previously published methods utilizing DC voltage, ferrofluid actuation has the benefit of providing electrical isolation between the tuning mechanism and the tunable element. Furthermore, we show in this work that magnetic actuation of ferrofluid allows for continuous tuning across frequency with a permanent magnet bias, as opposed to conventional magnetic tuning methods which normally require application of a variable magnetic field to a stationary load. Magnetic actuation of ferrofluid can be accomplished at a distance with a combination of magnets, and the system remains configured by the local bias magnet even after removal of the positioning field. Thus, magnetic tuning at a distance with ferrofluid offers a way to compensate for antenna package loading effects in situ. This work shows that magnetic tuning with a repositionable ferrofluid load has a broad range of applications in reconfigurable filter and antenna design.

Chapter 1

Introduction

Modern microwave systems must operate in spectral environments that are becoming ever more saturated. One technique utilized to avoid interference with nearby systems is cognitive radio [1]. Microwave systems using cognitive radio are able to detect which frequencies are currently in use in the vicinity, and adapt in real time to operate within available frequency bands [1]. Cognitive radio techniques benefit greatly from the use of components capable of operation over a wide range of frequencies [2]. As the front end of the microwave transmit/receive chain, the antenna typically has the greatest impact on the overall system noise figure when receiving because the antenna is the first element in the cascaded receiver network [3]. Consequently, an efficient tunable narrowband antenna results in a lower system noise figure than a broadband antenna cascaded with a filter, because the smaller bandwidth effectively filters out-of-band noise [4], reducing interference from neighboring systems operating at nearby frequencies [2]. A reconfigurable narrowband antenna can also have better efficiency and radiation characteristics at its operating frequency than a similar form factor broadband antenna with an operating bandwidth that matches the tunable bandwidth of the tunable antenna [5]. Thus, tunable narrowband antennas are particularly desirable in mobile applications where power and space are limited [4]. In addition to the performance advantages of tunable nar-

rowband operation, this work will show that a reconfigurable antenna can also be designed with the capability to compensate for loading effects due to the antenna's environment. Antennas rarely operate in an environment analogous to free space, so nearby objects have an effect on the reactive nearfield and the antenna's radiation and input impedance characteristics [5]. The antenna reconfiguration method presented in this work provides antennas with the capability to adapt in-situ to detuning effects due to the surrounding environment.

Many schemes currently exist for antenna reconfiguration: from loading with varactors [6]–[9], to stationary magnetic biasing of ferrite substrates [10]–[12], to use of "Micro-Electro-Mechanical System" (MEMS) switches and microfluidics [13]–[18]. Reactive loading with varactors or similar electrically-controlled devices often requires high DC voltages of up to 30 V or more, and additional design considerations such as RF chokes in order to isolate the RF and DC circuitry, resulting in increased design complexity [6]–[9]. Magnetically-controlled devices utilizing stationary biasing of ferrite materials offer inherent electrical isolation between the reconfiguration mechanism and the antenna, but require high magnetic field strengths which are most easily obtainable with permanent magnets [10]. The authors of [10] use a YIG (yttrium iron garnet) ferrite as a substrate, and spacers with a permanent magnet to vary the distance between the magnet and the substrate, effectively changing the strength of the bias field applied to the substrate [10]. The authors of [19] also use a special supporting structure to vary the distance between a permanent magnet bias and their antenna (Figure 1.2(b)). In practice, an electromagnet is desirable for continuous control of the field [10], but this is not practical for low power applications, as electromagnets require high currents in order to generate significant magnetic fields. The authors of [11] use an electromagnet to bias a patch antenna on a YIG substrate, but the bias field strength of the electromagnet

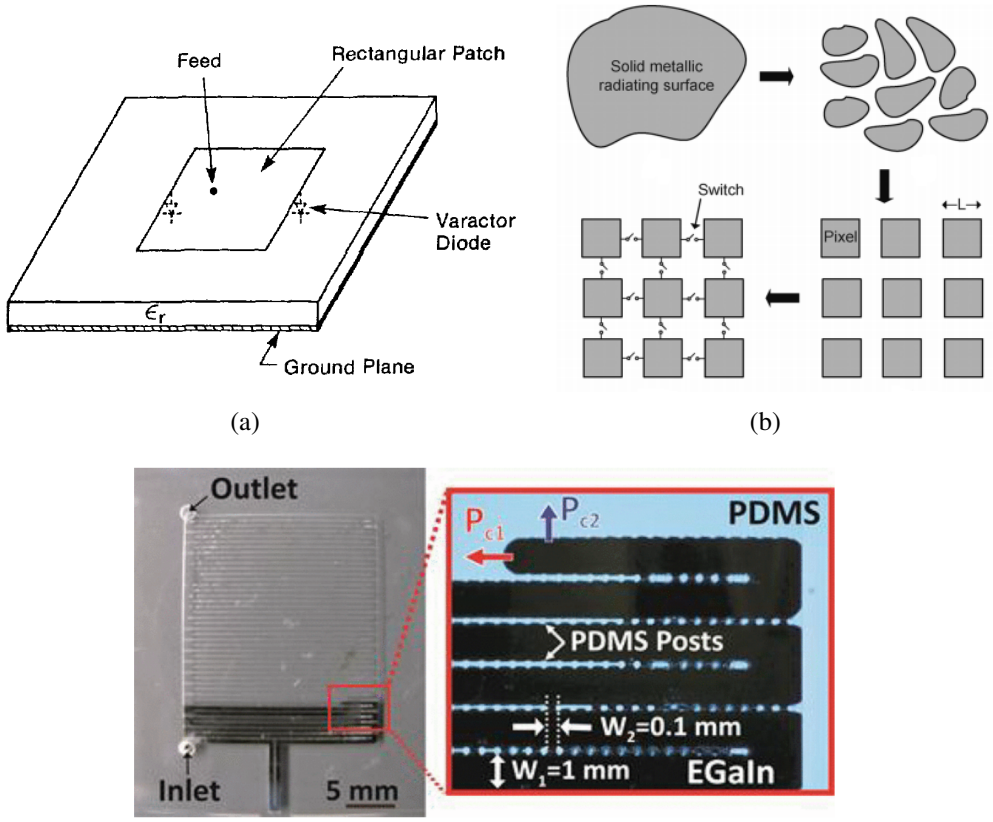

(a) (b)

(c)

Figure 1.1: Examples of electrical reconfiguration of antennas: (a) Tunable patch antenna end-loaded with varactors [6], (b) "Pixel" antenna utilizing MEMS switches [14], (c) Microfluidic patch antenna using conductive liquid alloy [15].

is limited to 48 kA/m. The tunable bandwidth is likely restricted by the limitations of the electromagnet, because the electromagnet is unable to deliver strong enough fields to bias the ferrite to its saturation magnetization of 100 kA/m [11]. Large tunable bandwidths can be obtained with MEMS technology, but antennas utilizing MEMS switches are typically not continuously reconfigurable, because the system operates by switching between discrete states (see Figure 1.1(b)) [13], [14], [20]. Microfluidic tuning is analogous to MEMS technology in that it involves physical relocation of a load, and it shows promise in applications where continuous tunability is desirable; however, a significant drawback is that microfluidic sys-

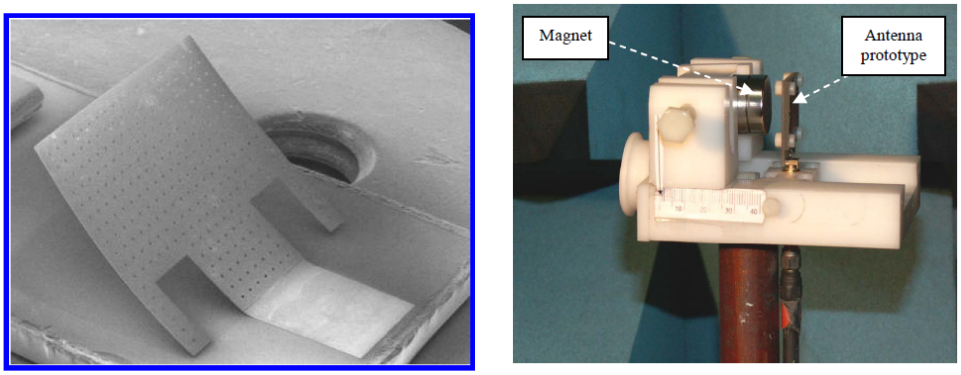

(a) (b)

Figure 1.2: Examples of magnetic tuning of ferrite-loaded antennas: (a) Tunable antenna using plastic deformation [21], (b) Tuning of a stationary ferrite with a variable magnetic field [19].

tems normally require a pump to reposition the fluid, increasing device complexity [16]–[18]. Additionally, microfluidic systems using liquid metal often suffer from oxidation-related issues that can inhibit repeated reconfiguration [17].

This work presents a novel method of tuning through magnetic control of a ferrofluid load. Magnetic tuning through actuation of a ferrofluid load avoids the issues normally involved in microfluidic tuning, because ferrofluid is a non-conductive material not prone to oxidation, and is attracted to a DC magnetic field. Thus, the fluid is repositionable through movement of an external magnetic "bias field" and does not require a pumping system. Additionally, the method presented in this work is preferable to voltage-controlled reconfiguration if high electrical isolation is desired between the tuning mechanism and the RF system. The magnetically-tuned system shown in this work does not require additional design considerations to prevent electrical interference between the tuning mechanism and the RF circuitry because the tuning mechanism is magnetically coupled with the RF system and thus inherently electrically isolated. Finally, this method of tuning can be accomplished at a distance with the combination of a permanent magnetic bias which

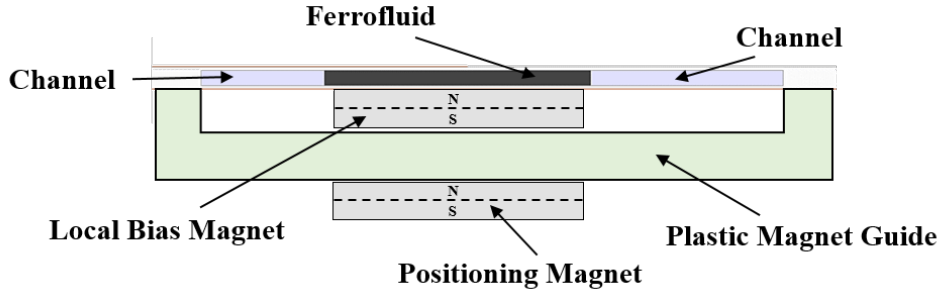

Figure 1.3: Diagram of repositionable ferrofluid load. Upon application of an external positioning field, the local bias is pulled away from the fluid such that it can move along the length of the plastic guide. After removal of the positioning field, the local magnet is again attracted to the fluid and kept in place with friction.

remains localized on the device, and an external magnetic positioning field (Figure 1.3). Upon removal of the external field, the local permanent magnet is attracted to the ferrofluid in the channel and remains in place due to the attraction between the materials and friction between the magnet and the ground plane. This tuning method combines both the advantages of magnetic tuning and microfluidic configuration without the inherent drawbacks normally present in each, and provides a way to compensate for device packaging effects without an applied voltage or physical access to the device. Furthermore, the presented method of magnetic tuning is advantageous because it does not require a controlled power source when done with permanent magnets, and offers a continuous tuning range that does not require placement of spacers between the permanent magnets and the device or a high power electromagnet, in contrast to [10] and [11]. Finally, this work presents a method of magnetic actuation of a physically repositionable load that allows for simple continuous tuning across the tunable range, as opposed to some methods like [13] and [20], which use electrical or magnetic forces to actuate a mechanical switch between discrete modes of operation.

An overview of magnetic tuning methods is given in Chapter 2. Conventional magnetic tuning is typically accomplished through biasing of ceramic ferrite materials, so an investigation of ferrite magnetic behavior and tuning methods is presented. Several soft ferrite testing methods were attempted in an effort to better understand magnetic biasing mechanisms, and these results are shown in Section 2.3. Chapter 3 presents an analysis of ferrofluid at microwave frequencies. In Section 3.3, a testing method for characterizing magnetic fluid behavior under varying magnetic bias strengths is demonstrated. Electromagnetic properties of several ferrofluids under a range of magnetic bias strengths from 0 to 74 kA/m and frequencies from 200 MHz to 5 GHz were measured, and the results are shown in Section 3.4. Chapter 4 introduces the novel method of magnetic reconfiguration proposed by this work in the form of a tunable microstrip stub element. Since the proposed ferrofluid-based tuning mechanism involves fluid volumes on the order of milliliters and dimensions on the order of millimeters, the proposed device is not a Micro-Electro-Mechanical System, but rather a "Milli-Magneto-Mechanical System". A simple transmission line model for the tunable microstrip element is present in Section 4.2, and a comparison between the modeled, simulated, and measured results is given in Section 4.3. Chapter 5 proposes several tunable patch antenna designs based on the tunable element demonstrated in Chapter 4. Patch antennas are designed with the aid of a transmission line model, and simulated, measured, and predicted performance of the antennas in free space is presented. To demonstrate impedance reconfigurability, results are shown for two different superstrates covering the improved tunable patch antenna design in Section 5.4. Chapter 6 demonstrates a tunable slot antenna design based on the same tunable stub mechanism where the microstrips are coupled to the slot, and a transmission line model for the slot antenna is developed and compared with simulation. Finally, Chap-

ter 7 presents conclusions and directions for future research involving tuning with magnetically-actuated ferrofluid loads.

Chapter 2

Magnetic Tuning With Ferrites

2.1 History and Theory of Magnetic Tuning

Historically, magnetic tuning has been accomplished through stationary biasing of ceramic ferrites. These methods usually suffer from higher losses due to the larger conductivity of ferrite materials compared to typical low-loss substrates [2]. One ferrite often utilized at microwave frequencies due to its lower loss is Yttrium Iron Garnet (YIG) [22]. As shown by Figure 2.1, increasing the strength of the biasing field effectively increases the resonant frequency of YIG, reducing its loss at lower frequencies, and also modifying the real part of the magnetic permeability [22]. YIG is just one example of a ferrite, but it demonstrates a typical property of ferrites where the resonant frequency shifts upwards as the bias field strength is increased. As shown in Chapter 3, a similar effect is also exhibited by ferrofluid. There are two main classifications of ferrites: "Hard" and "Soft". This classification is essentially a measurement of how easily the magnetic domains can change alignment, and is best visualized through the material's hysteresis curve (Figure 2.2) [23].

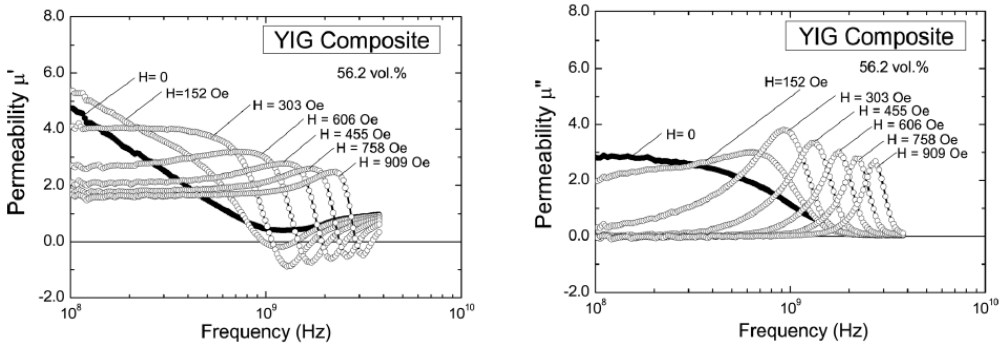

(a) (b)

Figure 2.1: Real and imaginary permeability values of YIG composite under varying bias fields and frequencies [22]. The maximum bias strength tested by the authors is 72.4 kA/m (One Oersted equals 79.6 A/m).

Soft ferrites have tall and narrow hysteresis loops, indicating that they exhibit a large change in magnetic flux density as a magnetic field is applied. Hard ferrites have wider hysteresis loops, meaning that a larger coercive field is required to override their remanent magnetization. As one might expect, hard ferrites behave more like permanent magnets than soft ferrites. The hysteresis curve is a convenient way to visualize the change in magnetic permeability μ as a function of the applied magnetic field intensity, and also the resulting magnetic flux density. The permeability is represented by the slope of the hysteresis curve, and the magnetic flux density is represented by the resulting $\vec{B}$ value. The flux density in the material, $\vec{B}$, is defined as

$$\vec{B} = \mu_0(1 + \chi_m)\vec{H} = \mu_0\mu_r\vec{H} = \mu\vec{H} \tag{2.1}$$

where μ_r represents the relative permeability of the material and $\vec{H}$ is the applied field intensity [24]; in general, μ_r is a nonlinear function of $\vec{H}$ [24]. This nonlinear behavior is often exploited to enable magnetically tunable devices through applica-

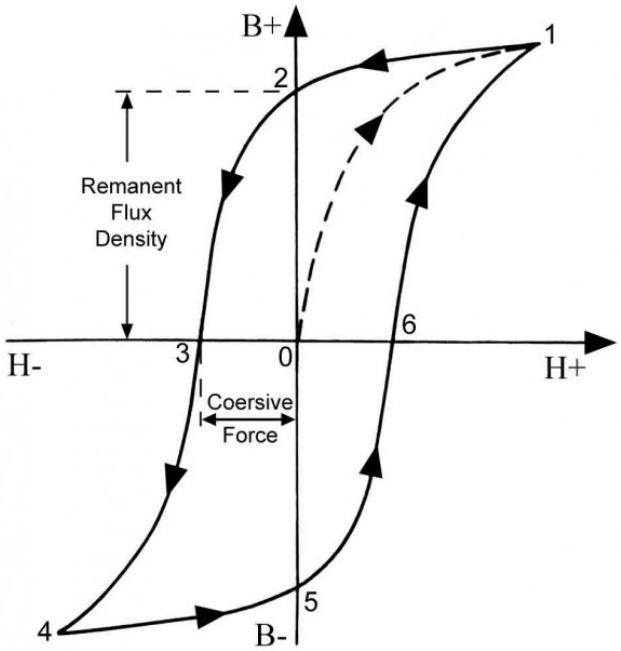

Figure 2.2: Typical hysteresis loop of a ferrite [25]. The H axis represents the magnetic field intensity applied, and the B axis represents the resulting magnetic flux density in the ferrite. Soft ferrites have tall and narrow hysteresis loops, and hard ferrite hysteresis loops are short and wide.

tion of a magnetic "bias field" which changes the permeability and hence modifies the phase velocity of a wave traveling through the material [24]. This behavior, combined with low conductivity, gives ferrites wide applicability at high frequency as phase shifters and inductive cores [24].

The point where the hysteresis curve intersects the horizontal axis is called the coercive field intensity, which is the intensity of the magnetic field necessary to break the alignment of the ferrite's magnetic domains and reorient them in a different direction [24]. As field strength increases above the coercive field intensity, the magnetic flux density follows the hysteresis curve up to its maximum value where it hits saturation: the point where any further increase in applied field does not result in an increase in magnetic flux in the ferrite [24]. After removal of the applied field in a magnetic material, the flux density will decrease along the hysteresis curve un-

til it hits its “remanent flux density”, which is the point of intersect with the vertical axis; this point is the inherent magnetization of the material that remains after the biasing field is removed, and thus it represents the strength of a permanent magnet’s flux density [24].

2.2 Stationary Ferrite Loading Experiments

We began our initial investigation by loading combinations of soft and hard ferrites onto a rectangular slot antenna in different configurations in order to determine the magnetic characteristics that would be most advantageous and potentially allow for antenna reconfiguration at a distance. Both soft and hard properties were desirable to enable reconfiguration at a distance, because the ferrite must have a tunable permeability and also exhibit remanance in order to remain configured after removal of the bias. The goal of this initial investigation was to determine more clearly the magnetic properties desired in a custom-sintered ceramic with both soft and hard properties by using the results from a well-characterized antenna as a starting point. Due to the required time investment and the difficulties in sintering ferrite ceramics, we first attempted magnetic tuning with a combination of commercially-available ferrites.

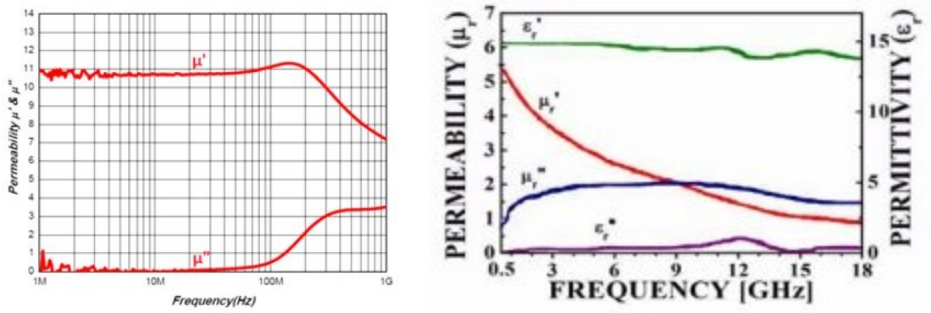

(a) (b)

Figure 2.3: Performance of soft ferrite absorber materials from Kitagawa Industries [26]: (a) IM-02 RF absorber, (b) NSSR-10G RF absorber.

The soft ferrite materials used to load the antenna were obtained from Kitagawa Industries [26]. These soft ferrite sheets are designed to work as RF absorbers at frequencies above UHF, but they have useful soft magnetic properties in the UHF range below 1 GHz (see Figure 2.3). As the provided data indicates, the NSSR-10G material should have a relative permeability in the range of $\mu_r = 5$ at 700 MHz, and the IM-02 material should have a permeability in the range of $\mu_r = 8$ at 700 MHz. Thus, the permeability varies as a function of both the applied field strength and frequency. Above 700 MHz, these materials begin to exhibit significant magnetic loss tangents. The soft ferrite materials were loaded onto the ends of a rectangular slot antenna in various combinations, as shown in Figure 2.4.

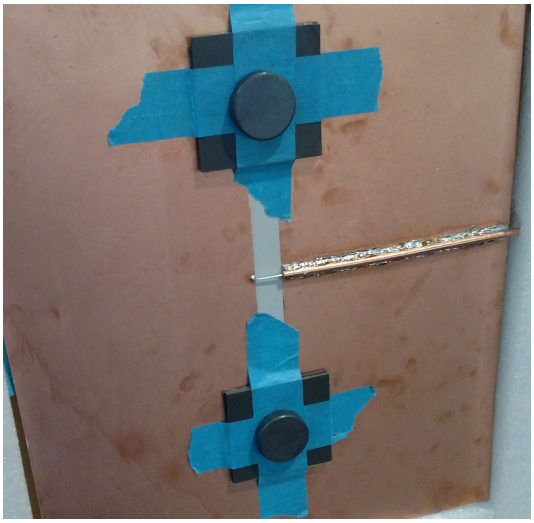

Figure 2.4: Simple rectangular slot antenna loaded with NSSR-10G material squares and biased with hard ferrite permanent magnets. The slot is 160 mm long, 12 mm wide, and fabricated on a 60 mil Rogers RO3006™ substrate. The antenna is center-fed with a coaxial feed configured as a Dyson-like balun [27].

Figures 2.5 and 2.6 show results for a few notable tuning configurations of the rectangular slot antenna. As the results in Figure 2.5 show, changing the placement of a magnetic bias results in tuning of the slot resonant frequency between 650 and 750 MHz. Application of different sizes and strengths of biases to the same location, as shown in Figure 2.6, results in an even larger tunable range from approximately 550 to 700 MHz.

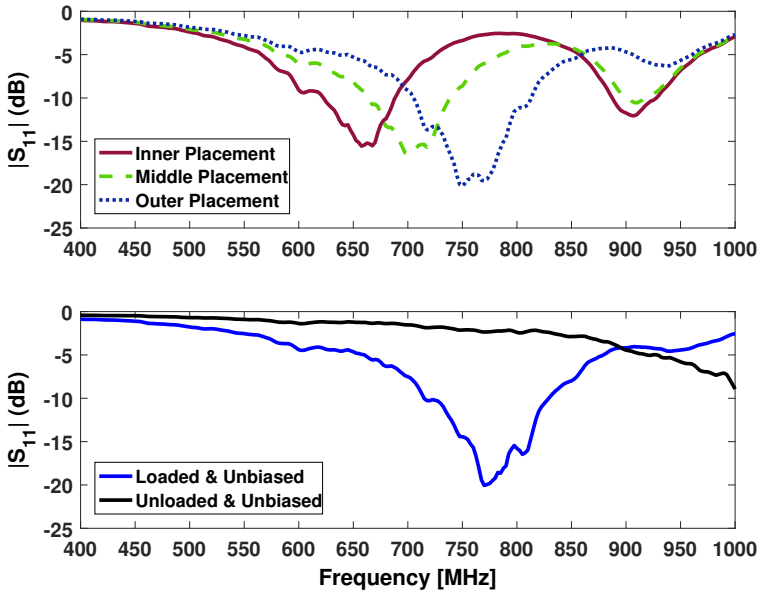

Figure 2.5: Tuning effect of a changing magnetic bias field on the stationary NSSR-10G end loads. Modification of the bias location on the end load relative to the center of the slot tunes the antenna between 650 and 750 MHz.

Tuning effects only remain as long as the permanent magnetic bias remains in place, indicating that changing the physical placement of the bias on a magnetic load also has the potential to tune the resonant frequency of an antenna. The bias magnets are hard ferrite ceramics, and thus they also have a dielectric loading effect on the ends of the slot. In order to better characterize the operation of the antenna, several tests were done on the ferrite materials, and results are presented in the next section.

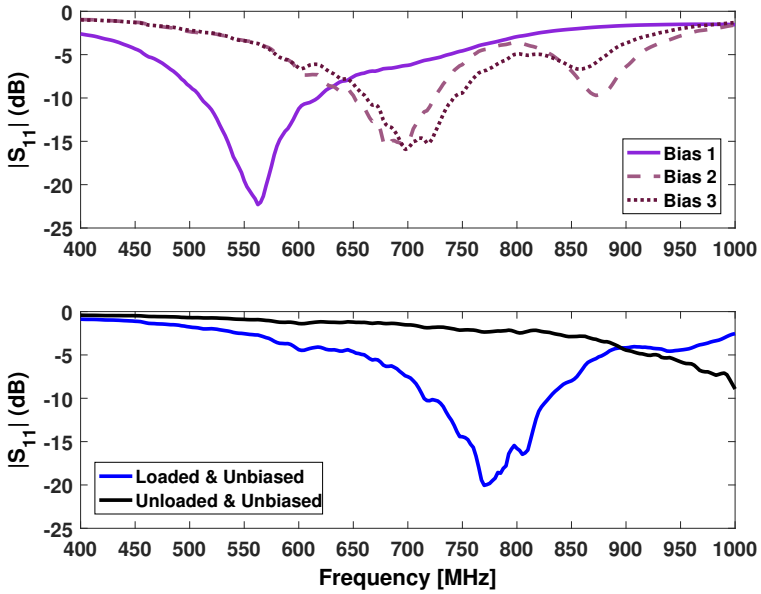

Figure 2.6: Tuning effect of a changing magnetic bias field strength on the stationary NSSR-10G end loads; Bias 1 is the strongest, and Bias 3 is the weakest. Modification of the bias intensity on the end loads tunes the antenna between 550 and 700 MHz.

2.3 Ferrite Material Testing

A testing method was devised to extract the permittivity and permeability data from the ferrites provided by Kitagawa, both to confirm the provided data and to test at frequencies outside of the given range. The soft ferrites are sheets, so they are not well-suited to testing in a coaxial measurement system. In addition, testing with a waveguide measurement system is impractical at frequencies below the R band because the physical dimensions become prohibitively large. Thus, a testing method based on slotline loading was developed. In order to form a better theoretical model for how these materials behave as antenna loads, characterization of the materials

was attempted in the slot antenna's frequency range of operation (0.4 – 1 GHz). A method to determine the frequency-dependent permittivity and permeability of the sheets was developed using slotline loading and Cohn's method to analyze the loaded slot [28], [29]. Three slotline standards were fabricated for TRL calibration of a network analyzer such that the line standard could be loaded with a test material. Analysis of this method and data is presented in the next section. Additionally, testing of the hysteresis curves was attempted, and this analysis is presented in Section 2.3.2.

2.3.1 Slotline Testing of Ferrite Materials

Slotline TRL calibration standards were fabricated using a 60 mil Rogers RT/duroid® 5880 substrate with a slot offset 20 mm from the center to improve the current-balancing effect of the feed [27]. In order to ensure high accuracy in the measurements obtained from this setup, the standards were fabricated to have the same electrical length to the edge of the sample holder section (outlined center section on the "Line" standard in Figure 2.7(b)).

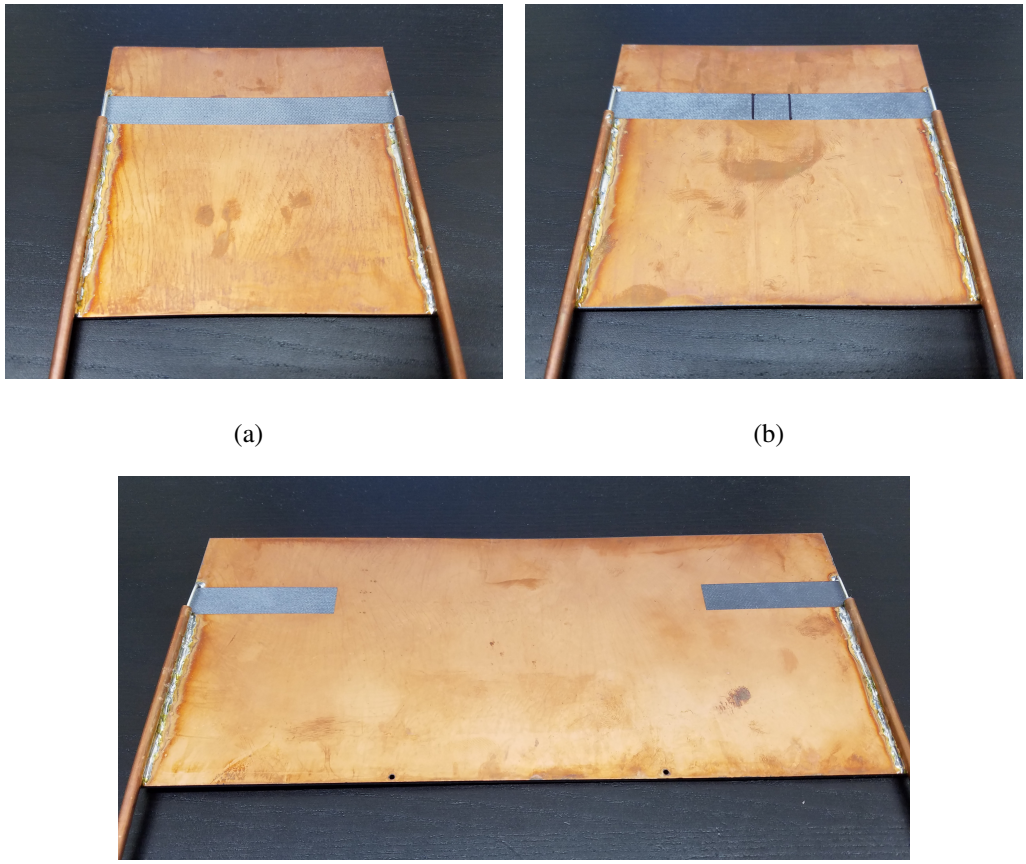

(a) (b)

(c)

Figure 2.7: Slotline TRL calibration standards: (a) Thru standard, (b) Line standard, (c) Reflect standard. The standards calibrate the network analyzer to the sample plane marked by the black lines in (b).

Even a small difference in coaxial feed length on the order of 1 mm has a notable effect on calibration accuracy. Group delay comparison can be used to determine the material's electromagnetic characteristics. A material with a large permittivity or permeability will shorten the effective wavelength and reduce the phase velocity of the wave as it travels down the line, resulting in a longer delay. In order to reliably determine the properties of the load, high precision is required in the TRL calibration due to the small variance in group delay that results from changing the

superstrate's properties. Figure 2.8(a) shows a surface plot of the effective wavelength in the slot as a function of both frequency and relative permittivity calculated with Cohn's method [28], [29]. The relative permeability is set to unity in order to reduce the number of variables. As the plot shows, the effective wavelength varies as a function of relative permittivity of the material loaded onto the slot line. This variation in wavelength results in a small change in group delay as the quasi-TEM wave propagates across the sample (Figure 2.8(b)). In order to test an unknown material, the calculated group delay using Cohn's method must be matched to the measured group delay from the slotline measurements.

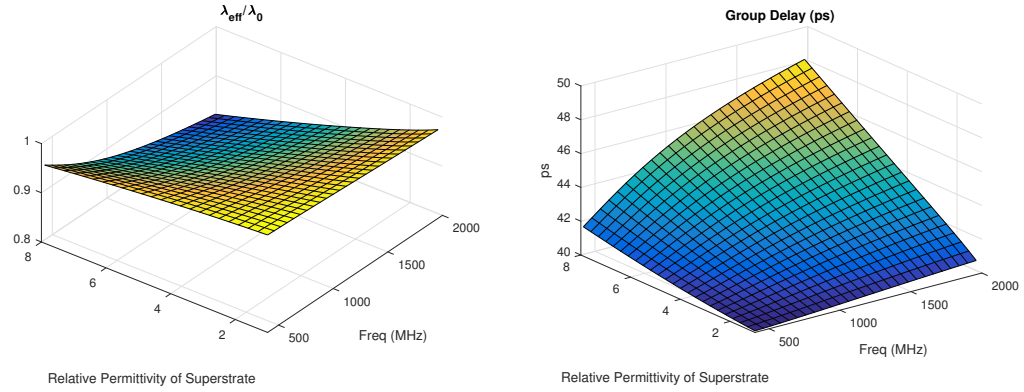

(a) (b)

Figure 2.8: Effective slot wavelength normalized to free space wavelength, and calculated group delay using the effective wavelength when a 60 mil superstrate of varying dielectric constant is placed over the slot: (a) Effective slot wavelength, (b) Calculated group delay.

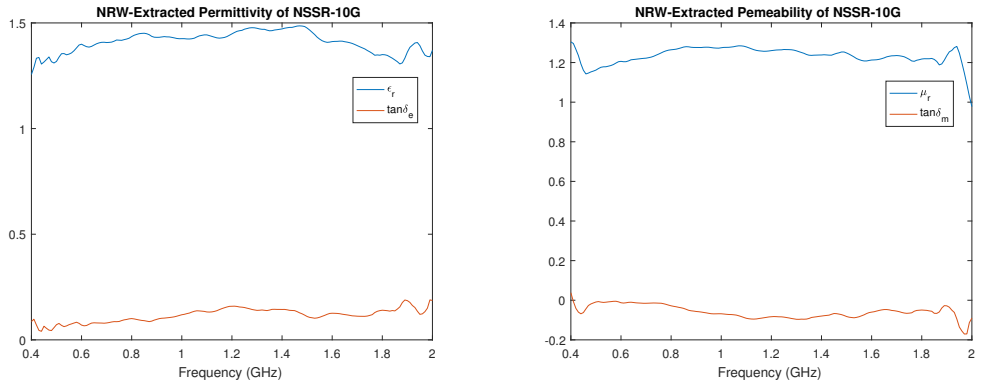

(a) (b)

Figure 2.9: Measured electromagnetic behavior extracted with application of the NRW algorithm to a 1 mm thick 12x12 mm sheet of NSSR-10G tested on the slotline measurement system: (a) Relative permittivity, (b) Relative permeability.

An initial guess is made for the material properties of the slotline load using the Nicholson-Ross-Weir (NRW) algorithm, which is accurate for most coax and waveguide measurement systems [30], [31]. This guess is then used to determine the starting point for a range of values for the property, which are each evaluated using Cohn's method for a sandwich slotline in order to determine the effective wavelength in the slot as a function of the material parameters [28], [29].

The plots in Figures 2.9(a) and 2.9(b) represent properties extracted using the NRW algorithm, which is not designed to be applied to a loaded slotline. However, as shown by the extracted data, the algorithm still returns physically reasonable results for the material, though the extracted permeability values are markedly lower than those given by the Kitagawa-provided datasheet for NSSR-10G (Figure 2.3(b)). The NRW-extracted data represent a starting value for a range of test values loaded into Cohn's iterative process in order to determine the effective wavelength and group delay of the wave in the slot. Then, the measured group delay of the sample can be compared with the theoretical value in order to determine the loading effect

of the sample on the slot.

Unfortunately, the test setup was not precise enough to measure the material properties accurately. A 1 mm change in transmission line length in the coaxial feed results in a time delay change on the order of 5 ps. This is too much error for the method to work accurately with the current set of slotline standards, because as shown in Figure 2.8(b), loading the slot with a superstrate with $\epsilon_r = 8$ only results in a delay change of roughly 7 ps compared to a load with $\epsilon_r = 1$ (for a 60 mil superstrate). Increasing the thickness of the load to 180 mil results in the calculated delay shown in Figure 2.10(b). As Figure 2.10(b) shows, increasing the superstrate (sample) thickness does result in an increase in group delay variance for the entire setup, but the change in group delay as a function of permittivity of the load is still not large enough to significantly reduce the potential errors resulting from slight line length differences.

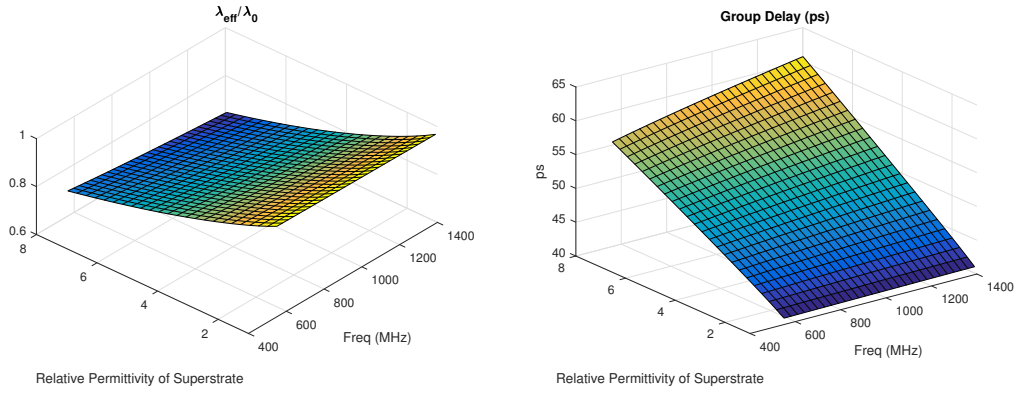

(a) (b)

Figure 2.10: Effective slot wavelength normalized to free space wavelength, and calculated group delay using the effective wavelength when a 180 mil superstrate of varying dielectric constant is placed over the slot: (a) Effective slot wavelength, (b) Calculated Group Delay.

For a line length difference on the order of 1 mm, the potential for error is nearly 25% for the 180 mil loaded superstrate. In order to improve the accuracy of this testing method, the slotlines must be fabricated to a very high degree of precision, and the superstrate load must be positioned precisely in the same location on the line for each measurement. Slotline testing of ferrite sheet materials has potential, but suffers from inaccuracies due to the small uncertainty in the electrical lengths of the coaxial feeds soldered onto the TRL test standards (Figure 2.7). Reasonable accuracy was not obtainable with the fabricated slots, so another method, presented in the next section, was developed to determine the hysteresis curves and permeability of the ferrites.

2.3.2 Hysteresis Testing of Ferrite Materials

In order to determine the full hysteresis curve of a magnetic material, the applied magnetic field intensity must be strong enough to overcome the material's inherent coercive field intensity. In order to test the ability to "overwrite" the hard ferrites for hysteresis characterization, a test setup was devised to apply a large DC current opposing the magnet's remanent flux density (Figure 2.11). Voltage is applied to the coil such that its magnetic field opposes the polarity of the magnet's remanent field according to the Right Hand Rule [24]. The floating magnet on top will drop if the current through the coil on the bottom magnet is strong enough to overcome the bottom magnet's remanent flux density.

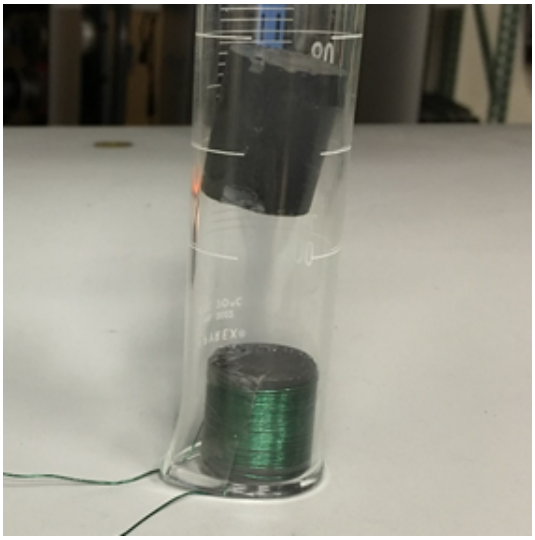

Figure 2.11: Test setup for attempted re-biasing of hard ferrites. Current is applied to the coil on the bottom magnet to oppose its remanent field such that any change in the distance between the magnets indicates a change in the flux density of the bottom magnet.

At a coil current of 10 amps, the magnetization of the bottom magnet showed no change. A stronger current was not attempted due to heating of the coil and the magnet – after 15 seconds of 10 amps being applied, the temperature of the magnet exceeded 115 degrees Fahrenheit (46 degrees Celsius). Hysteresis testing of hard ferrites requires high power levels because the coercive field intensity must be overcome on each cycle of the applied current wave. If the applied H field is not strong enough to realign the ferrite's magnetic domains and reverse the remanent flux density with each cycle, the resulting plot will not show the hysteresis of the material; hence, no further work was attempted to determine the hysteresis curves of the hard ferrites.

The soft ferrites have lower coercive field intensities, so hysteresis testing is more practical than with the hard ferrites. First, strips of both NSSR-10G and IM-02 were cut, stacked, and wrapped to form square cross-section toroids as in Figure 2.12(b). The toroids were then wrapped with primary and secondary windings of magnet wire as in Figure 2.12(a). This formed a transformer with the stacked soft ferrite sheets as the core, theoretically allowing calculation of the hysteresis of the material through measurement of the difference in input and output voltages to the two coils. One coil was used to excite the ferrite core, and the second was inductively coupled to the first through the core. The hysteresis curve, which is a function of the core's permeability, was then be extracted. Hysteresis becomes difficult to measure at higher frequencies for several reasons: The Tektronix AWG7122C signal generator used to generate the primary side voltage can output frequencies up to 6 GHz. At 700 MHz, only 17 points are generated per cycle of the sine wave, resulting in high-frequency noise in the measurements and reducing their precision. Furthermore, the signal generator can output a maximum voltage of 1 V_{pp}.

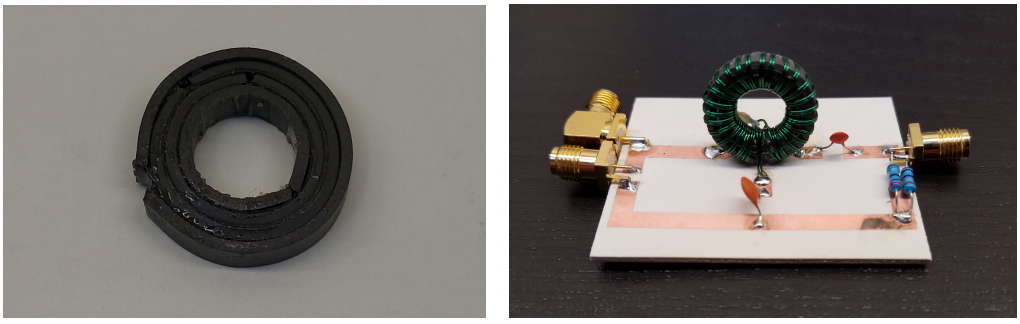

(a) (b)

Figure 2.12: Measurement of soft ferrite toroid. Soft ferrite sheets are cut into 4 mm wide strips, layered, and curved to form a 4 mm square cross-section toroid: (a) Close-up picture of toroid, (b) Toroid wrapped with coils on measurement circuit.

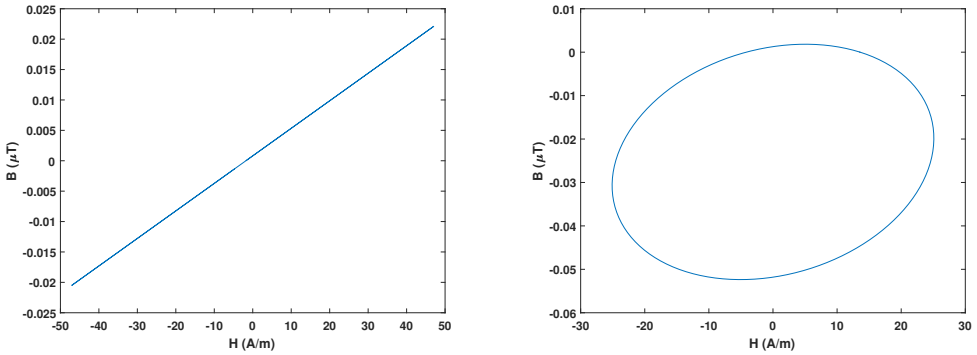

(a) (b)

Figure 2.13: Measured hysteresis curves for the IM-02 toroid: (a) 700 MHz, (b) 400 MHz. The curves indicate that not enough power is being delivered to the toroid to induce a measurable hysteresis effect in the material.

At a characteristic impedance of 50 Ω, this is equivalent to only 2.5 mW of time-averaged power, which is likely not enough to drive the soft ferrite material into magnetic saturation. Finally, the reactance due to the capacitance between the windings becomes significant at higher frequencies. Coil capacitance is unavoidable even when the windings are touching, due to the circular cross-section of the wire. These effects reduced the accuracy of the measurements, but testing was still attempted in order to obtain a better idea of the shape of the curve and expected values.

Hysteresis curves were determined using curve-fitted data from the Tektronix DPO70G04 oscilloscope. The measured hysteresis curve for the IM-02 material at 700 MHz is plotted in Figure 2.13(a). In order to illustrate the frequency dependency of hysteresis, the IM-02 hysteresis curve was also measured at 400 MHz. The plot in Figure 2.13(b) is closer in shape to what is expected for a hysteresis curve; however, the absence of saturation points in the first and third quadrants (points 1 and 4 in Figure 2.2) indicates that the test setup is not delivering enough power to drive the material into saturation. Figure 2.13 indicates that the cited inaccura-

cies inherent to the test setup are too significant for accurate measurement of the materials.

2.4 Conclusions

Loading a rectangular slot antenna with ferrite material has the potential to enable magnetic tunability. However, tuning of the antenna at a distance was not possible because the loading ferrite's permeability only stayed configured as long as the bias magnet remained in place. Furthermore, ferrites are difficult to characterize in the desired frequency range, and are limited in frequency by their loss. Magnetic behavior, being inherently nonlinear, is difficult to model and measure. These factors combined make predictable, continuous magnetic tuning at a distance through stationary biasing of ferrites impractical for the targeted application. However, as the stationary biasing results in Figure 2.5 show, changing the location of a bias field on a stationary ferrite has a tuning effect on the antenna. This tuning is due to both biasing of the magnetic material, and the bias magnet itself working as a repositionable load. In order to implement tunability at a distance, magnetic actuation of a movable load is more likely to be effective than stationary loading, because if the load can be moved magnetically, it will remain in place after removal of the positioning field due to the magnetic attraction between the local bias and the loading material. This conclusion was the impetus for the development of a tunable system using magnetically-actuated ferrofluid following the schematic shown in Figure 1.3. The rest of this work is focused exclusively on magnetic actuation of ferrofluid in order to tune a variety of structures.

Chapter 3

Magnetic Reconfiguration With Ferrofluid

3.1 Ferrofluid-Based Devices

Ferrofluid is a magnetically-reactive liquid originally developed by NASA as a fluid that could be manipulated in a zero-gravity environment [32]. It typically consists of magnetic particles with a diameter of approximately 10 nm suspended in an oil-based solution [33]. Water-based solutions also exist, but tend to be problematic, as the suspended particles are more prone to formation of aggregates over time [34].

Ferrofluid has been used in reconfigurable devices at frequencies below UHF. As demonstrated by [35], ferrofluid is useful as an inductive load (Figure 3.1). The authors in [35] use a variable magnetic bias field to change the spatial distribution of the fluid over the coil, effectively changing the inductance of the device by modifying the magnetic loading of the coil [35]. Practical operation of the device is limited to frequencies lower than 300 MHz, because at higher frequencies the inductance does not change significantly as a function of the bias field [35]. Ferrofluid also finds application in sensing devices. One such device uses magnetic loading due to the movement of ferrofluid in an inclinometer (Figure 3.2) [36]. The device senses a change in its angle of incline when gravity causes the ferrofluid to move, changing the magnetic field sensed by the Hall Effect sensor [36].

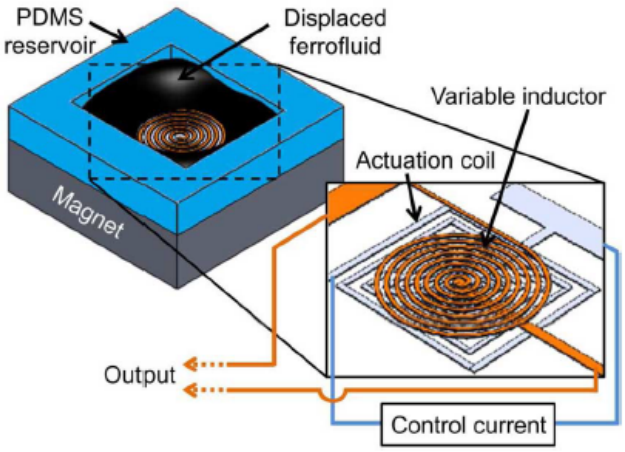

Figure 3.1: Ferrofluid-based variable inductor designed by [35].

Another application of ferrofluid is in the optical range of frequencies [37]. In [37], a fiber coupler is made reconfigurable through application of ferrofluid (Figure 3.3). The coupler operates at optical frequencies where absorption is high, so rather than utilizing ferrofluid as a variable load, the authors take advantage of the high absorption and employ a "laser-induced thermal effect" to shift the refractive index of the fluid as a function of the laser's power [37].

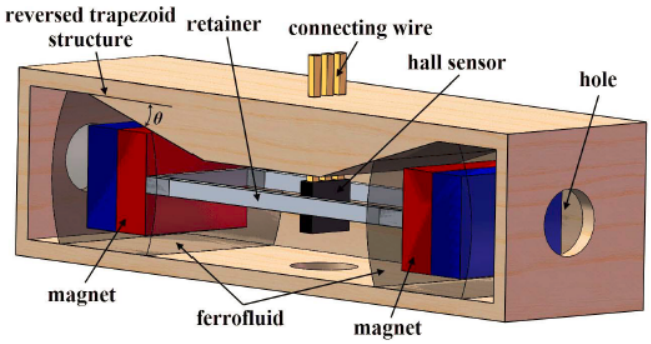

Figure 3.2: Ferrofluid-based inclinometer designed by [36].

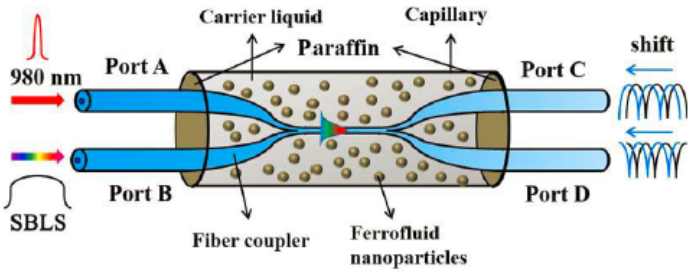

Figure 3.3: Optically-tunable fiber coupler designed by [37].

Many conventional reconfigurable devices utilizing ferrofluid exploit the fluid's magnetic effects. This limits usage of the fluid to frequencies lower than UHF because the magnetic loss tangent increases significantly as a function of frequency. However, as shown in the next section, application of a strong permanent magnetic bias field increases the resonant frequency of ferrofluid and significantly reduces its magnetic effects at lower frequencies. This enables low-loss ferrofluid loading at frequencies in the UHF range.

3.2 Ferrofluid Characteristics at UHF

The magnetic particles in ferrofluid have two main forms of relaxation: Brownian relaxation due to physical rotation of the particles in the carrier fluid, and Néel relaxation due to the spontaneous reorientation of the particle's internal magnetic moment [33], [38]. Since ferrofluid typically consists of particles with a diameter on the order of 10 nm, and the Néel relaxation time τ_N is an exponential function of particle volume [38] while the Brownian relaxation time τ_B is a linear function of volume [33], τ_N is typically much smaller than τ_B in ferrofluid [39]. Thus, the effective relaxation time

$$\tau_{eff} = \frac{\tau_N \tau_B}{\tau_N + \tau_B} \tag{3.1}$$

is dominated by the Néel relaxation time [39]. This is generally true for ferrofluids consisting of magnetite particles on the order of 10 nm [40]. This work focuses exclusively on magnetite-based fluids, so $\tau_N << \tau_B$ [40], and any shift in resonant frequency due to a magnetic bias field is due primarily to modification of τ_N. Magnetic biasing of ferrofluid has the effect of increasing the magnetic resonance frequency of the fluid through increasing the fluid's Néel relaxation time, so application of a bias field significantly reduces the relative permeability and magnetic loss tangent at frequencies much lower than the magnetic resonance [33], [41].

3.3 Ferrofluid Measurement Process

A coaxial test method based on the NRW algorithm [30], [31] was designed in order to characterize ferrofluid in the frequency range of 200 MHz - 5 GHz. The testing system consists of a coaxial test structure formed from modified N-type thru connectors from Pasternack (Figures 3.4 and 3.5(a)), in a similar method to the one detailed in [42]. To provide a variable DC magnetic bias for the fluid while under test, Helmholtz coils (Figure 3.5(b)) were fabricated to output up to a 74 kA/m DC magnetic field. This allowed for characterization of the ferrofluid at different frequencies under a variety of controlled bias conditions. The Helmholtz coils were wrapped around a 3D printed coil holder in the Brooks coil configuration in order to maximize their inductance [43]. The coils were separated by a distance greater than their radii, and thus were not in the ideal Helmholtz configuration. According to a study of optimum coil spacing in [44], magnetic field uniformity within 1% along the primary axis of the coils can be obtained even when the coils are separated by a distance up to 38% greater than the Helmholtz spacing. The fabricated coils were spaced at a distance 30% greater than their optimal Helmholtz spacing of 35.9

mm, so they produce less than a 1% variation in field strength between the coils. The sample holder was filled with ferrofluid, and then the response was measured on the network analyzer and the S-parameters were saved for each 5 kA/m step of magnetic bias field strength, up to 74 kA/m. In addition, a maximum bias field of approximately 134 kA/m was applied to the sample by two large Neodymium bar magnets. The field produced by the bar magnets varied from 130 kA/m to 138 kA/m within the sample volume, resulting in a spatial variation of roughly 6%, which was greater than the variation in the field due to the coils.

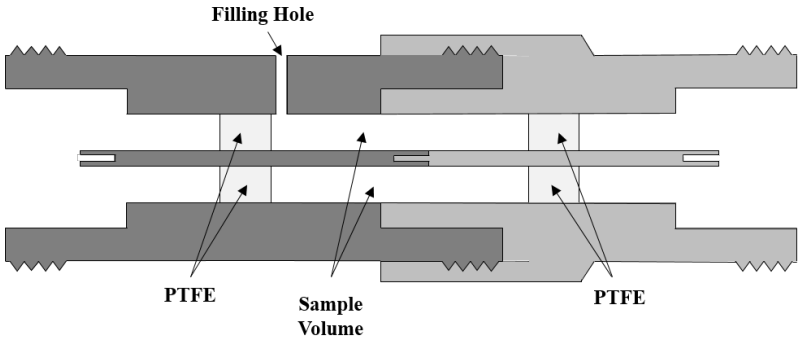

Figure 3.4: Side view of coaxial sample holder fabricated from two N-type thru connectors in a similar setup to the one used in [42]. Ferrofluid is filled through the filling hole into the region labeled "Sample Volume" between the connectors.

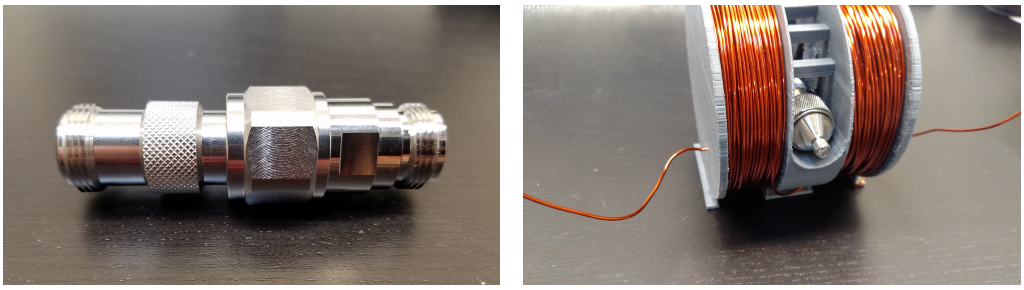

(a) (b)

Figure 3.5: Ferrofluid measurement system: (a) Sample holder composed of two N-type thru connectors from Pasternack, (b) Sample holder centered between the Helmholtz coils.

However, since the measured loss tangent peak in EFH1 occured around 5 GHz at the maximum bias field strength (Figure 3.8(b)), the uncertainty in measured data was small at frequencies much lower than the resonance. Several types of ferrofluid were tested, and all samples came from Ferrotec Corp. [45]. Magnetic fields were measured with the Allegro™ MicroSystems A1302 Hall-Effect sensor.

3.4 Ferrofluid Measurement Results

3.4.1 Oil-Based Ferrofluid

EFH1 is a well-characterized oil-based ferrofluid with a magnetic particle concentration of 7.9% and a saturation magnetization of 44 mT [46]. Surface plots of the dielectric and magnetic behavior of EFH1 are shown in Figures 3.6 and 3.7 respectively. Several trends are notable in these plots. Measurements confirm the expected behavior of ferrofluid under bias predicted by [41] and [33]. As shown in Figure 3.7(b), the peak in the magnetic loss tangent shifts higher in frequency as the magnetic bias field strength increases.

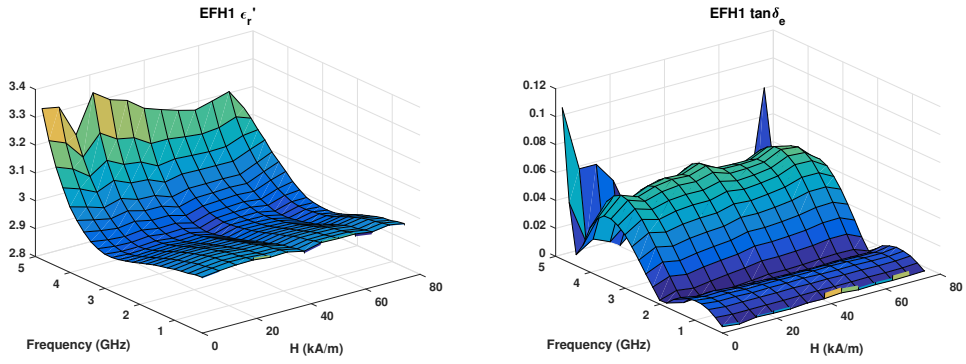

(a) (b)

Figure 3.6: Surface plots of measured dielectric effects of EFH1 ferrofluid over a frequency range of 200 MHz to 5 GHz, and a magnetic bias field strength range of 0 to 74 kA/m: (a) Real relative permittivity, (b) Dielectric loss tangent.

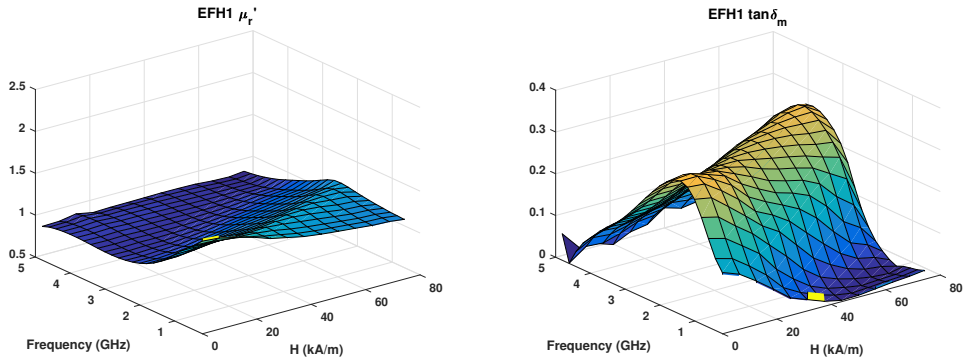

(a) (b)

Figure 3.7: Surface plots of measured magnetic effects of EFH1 ferrofluid over a frequency range of 200 MHz to 5 GHz, and a magnetic bias field strength range of 0 to 74 kA/m: (a) Real relative permeability, (b) Magnetic loss tangent.

Figure 3.8 shows the magnetic behavior of EFH1 across frequency both at zero magnetic bias, and at the maximum bias field strength. As shown by Figure 3.8(b), the magnetic loss tangent is reduced to below 0.05 below 2.5 GHz. Designs using ferrofluid as a load can exploit this behavior by applying an appropriately strong permanent bias field to the fluid. In addition, Figure 3.6 shows that, as expected, the measured dielectric behavior of the fluid is essentially independent of the bias field strength.

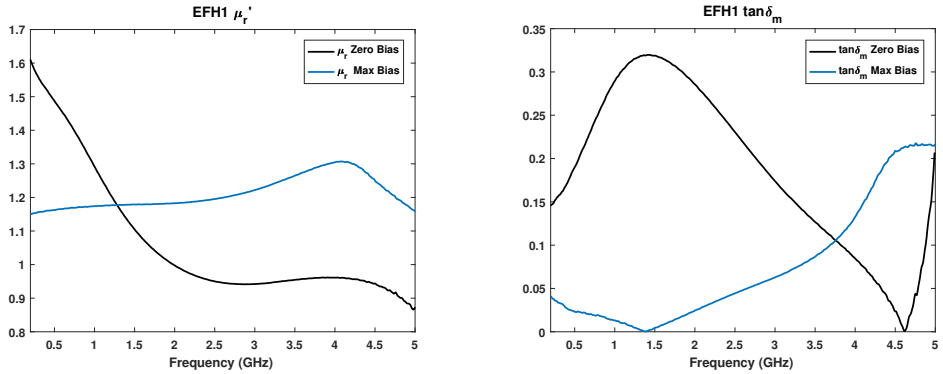

(a) (b)

Figure 3.8: Measured magnetic behavior of EFH1 at zero bias and at a maximum bias field strength of 134 kA/m: (a) Real relative permeability, (b) Magnetic loss tangent. At frequencies below 2.5 GHz, the maximum bias field significantly reduces the magnetic loss tangent and also reduces the real part of the relative permeability to a near constant value of 1.2.

EMG900 has a magnetic particle concentration of 17.7% and a saturation magnetization of 99 mT [47], so it exhibits a stronger attraction to the magnetic bias field than EFH1. As shown in Figure 3.9, the maximum strength bias field also increases the magnetic resonant frequency and reduces the loss tangent of EMG900 at lower frequencies. However, EMG900 also exhibits a higher loss tangent than EFH1, making it less efficient as a load. Ultimately, the choice of ferrofluid particle concentration is dependent on system requirements. For high efficiency designs, a low concentration is desirable in order to minimize loss. In some cases, certainty of fluid placement may be more important than high efficiency, so a higher particle concentration may be more advantageous. These results indicate that at maximum magnetic bias strength, both EFH1 and EMG900 can be modeled as movable dielectrics with a weak magnetic response at frequencies much lower than their magnetic resonances, simplifying the design and analysis process of devices loaded with oil-based ferrofluid.

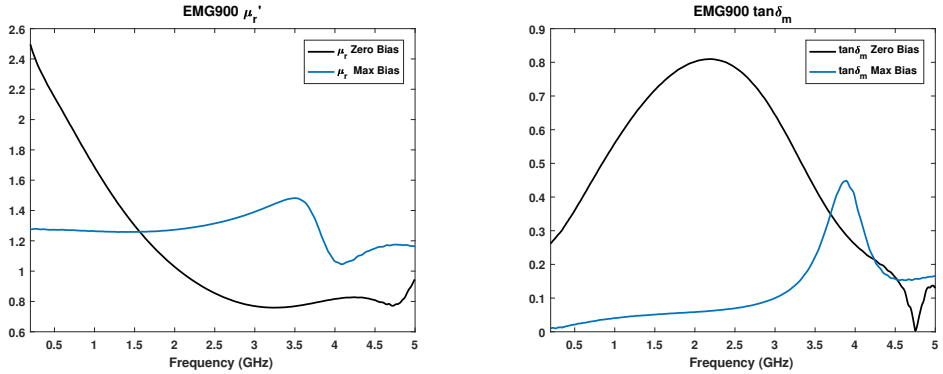

(a) (b)

Figure 3.9: Measured magnetic behavior of EMG900 at zero bias and at a maximum bias field strength of 134 kA/m: (a) Real relative permeability, (b) Magnetic loss tangent. At frequencies below 2.5 GHz, the maximum bias field significantly reduces the magnetic loss tangent and also reduces the real part of the relative permeability to a near constant value of 1.3.

3.4.2 Water-Based Ferrofluid

A water-based ferrofluid, EMG700 [48], was also tested. The dielectric constant of water-based ferrofluids is much higher than for oil-based fluids, meaning that the fluid will cause a much greater change in propagation velocity and wave impedance and potentially offer a larger tunable range. However, even under a bias strength of 134 kA/m, the measured dielectric loss tangent is far too high for the fluid to be useful as a low-loss load at microwave frequencies (Figure 3.10(b)). Additionally, water-based ferrofluids are more likely to form aggregates over time than oil-based fluids [34]. Due to their higher loss and lower stability, water-based ferrofluids were not incorporated into tunable designs in this work.

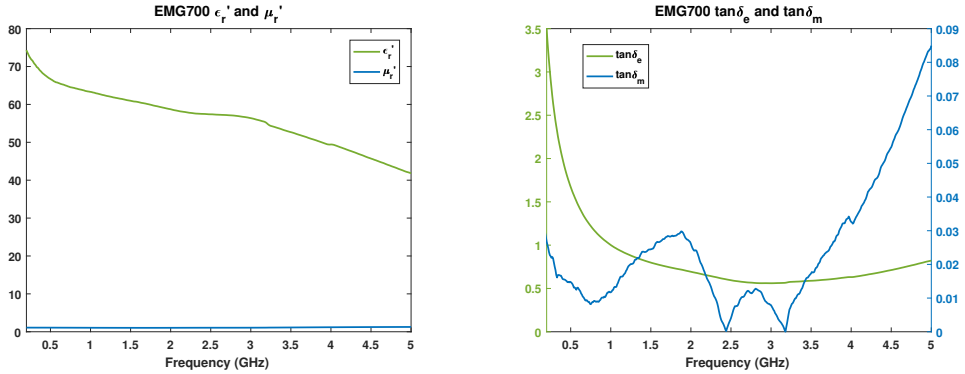

(a) (b)

Figure 3.10: Measured electromagnetic properties of EMG700 at the maximum bias field strength of 134 kA/m: (a) Relative permittivity and permeability, (b) Dielectric and magnetic loss tangents.

3.5 Conclusions

EFH1 ferrofluid shows potential as a low-loss load at microwave frequencies in the UHF range when under a strong magnetic bias. Analysis of devices using ferrofluid as a load under strong magnetic bias is simplified because the relative permeability of the fluid is significantly reduced by the bias field. As long as the ferrofluid is biased with a strong enough field and limited to operation below a frequency threshold, it behaves as a dielectric with a weak magnetic response dependent on the bias strength and the fluid's particle concentration. As shown in Figures 3.8 and 3.9, EMG900 has a higher loss tangent than EFH1 under an equivalent bias, which agrees with results from [49]. EFH1 has a lower particle concentration, but is still attracted strongly enough to a bias field to be repositioned; thus, EFH1 is a prime candidate for this tuning method because of its lower particle concentration and its oil base. The main trade-off in the design of ferrofluid-tuned devices is between efficiency and predictability. Too much reduction in particle concentration results in less attraction between the ferrofluid and the bias field, increasing the uncertainty

of the fluid's position. Since the fluid is modeled as a simple block of material in transmission line analysis (Section 4.2), any uncertainty in fluid placement reduces its accuracy.

EFH1 was chosen as a reasonable trade-off between mechanical mobility, loading effect, and loss. Below approximately 2.5 GHz, EFH1 has a magnetic loss tangent of approximately 0.05 or lower, and a dielectric loss tangent below 0.025 under a magnetic bias of 134 kA/m or higher. In the same frequency range, its real relative permeability is a near constant 1.2, and its dielectric constant is approximately 3. For the rest of this work, EFH1 is used exclusively as the ferrofluid load. The electromagnetic properties used in modeling and simulation are given by the measured properties at maximum bias shown in Figure 3.11.

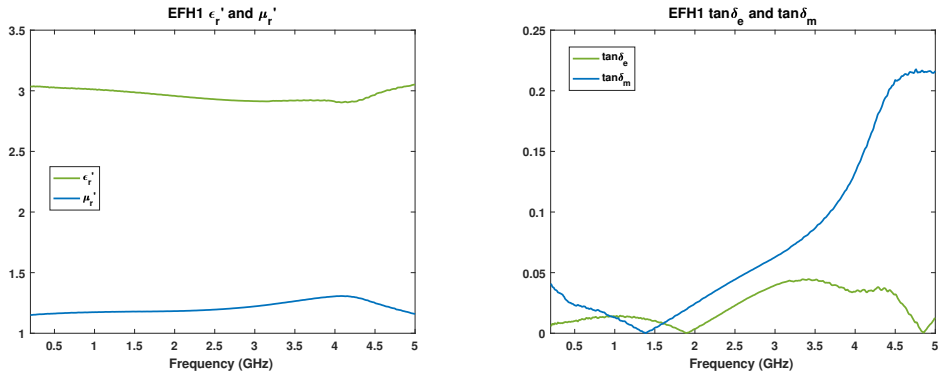

(a) (b)

Figure 3.11: Measured electromagnetic properties of EFH1 at the maximum bias field strength of 134 kA/m: (a) Relative permittivity and permeability, (b) Dielectric and magnetic loss tangents.

Chapter 4

Tunable Microstrip Stub Using Repositionable Ferrofluid Load

Microstrip circuits are ubiquitous in the world of RF engineering because of their ease of fabrication and planar nature [3]. A tunable microstrip element is easily integrated with existing microstrip circuitry, and with planar antennas like patches and slots. Loading ferrofluid in the substrate of a microstrip element ensures high electrical isolation, because the ferrofluid is repositioned with a magnet on the other side of the ground plane. The tunable element acts as a continuously tunable capacitive reactance when the microstrip length is less than or equal to $\frac{\lambda}{4}$ [24]. Tuning is accomplished through physical repositioning of a ferrofluid load, resulting in modification of the substrate properties of the stub and the microstrip's characteristic impedance and propagation constant. This complicates device fabrication somewhat because the load must be placed in a channel in the substrate in order to have a large impact on the electric fields of a microstrip circuit. However, the increasing prevalence of 3D printers with the ability to print multiple materials will facilitate easy fabrication of these tunable devices in the near future [50]. Some implications of 3D printer technology will be discussed in more depth in the final chapter.

Ferrofluid allows for tuning of a microstrip stub element when loaded in the substrate beneath the microstrip [51]. This design can be loaded onto several types of antennas as shown in Chapters 5 and 6, resulting in tunability of the antennas

through modification of the stubs. The electric fields in a microstrip transmission line are mostly confined to the substrate region between the strip and the ground plane, so modification of the substrate will have a large effect on the fields. The geometry of a microstrip line allows for easy placement and confinement of fluid in a channel, which can be repositioned through magnetic actuation from the other side of the ground plane. This has the added benefit of the tuning system being electrically isolated from the RF transmission line due to the ground plane. When loaded properly onto an antenna structure, the stub acts as a reactive load, meaning that the radiating fields are not directly affected by the ferrofluid. Thus, antennas loaded with ferrofluid in this manner have the potential to perform at higher efficiency than conventional magnetically-tuned antennas where the entire substrate is a magnetic material. Finally, the design is planar, and integrates easily with planar and conformal antennas such as patches and slots. The tunable microstrip stub was originally designed as a two port filter element in order to simplify testing and analysis of the input impedance characteristics of the stub. Due to the non-radiating nature of the structure and the ability to easily measure energy transmission through the system, testing was done solely on a network analyzer without the need for anechoic chamber testing.

4.1 Design and Fabrication

The microstrip element is a tunable stub designed to operate as a first order Butterworth lowpass filter, so the stub impedance is made to be half of the 50 Ω feed impedance [3]. Figures 4.1 and 4.2 show the design which consists of a single, tapered microstrip stub with a characteristic impedance of 25 Ω centered between the ports. The stub design impedance of 25 Ω requires a relatively large stub width

of 10.69 mm when placed onto a 70 mil Rogers RO4350B™ substrate, so the extra capacitance due to the width of the stub is mitigated with the addition of tapers at the stub attachment point as suggested by [52]. The filter element is fabricated using two substrate layers as shown in Figure 4.4. The bottom layer is 60 mil thick and is composed of the ground plane and a channel cut using a milling machine to the width of the stub, twice the stub length, and a depth of 50 mils. Using Devcon 5 Minute® epoxy, the bottom layer is bonded to a 10 mil thick top layer, onto which the microstrip design is etched using photolithography.

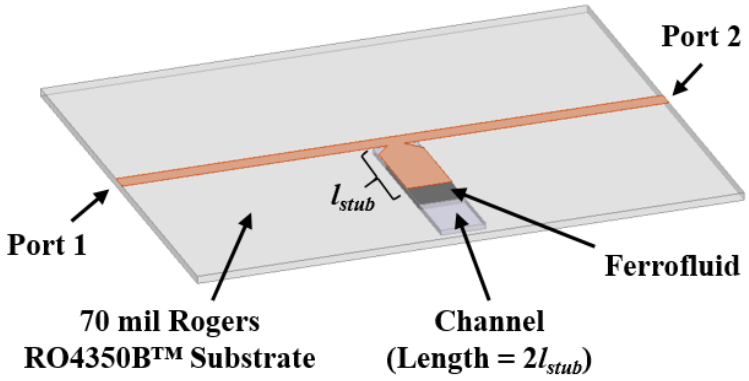

Figure 4.1: Top view of the tunable microstrip stub element loaded with a movable ferrofluid load.

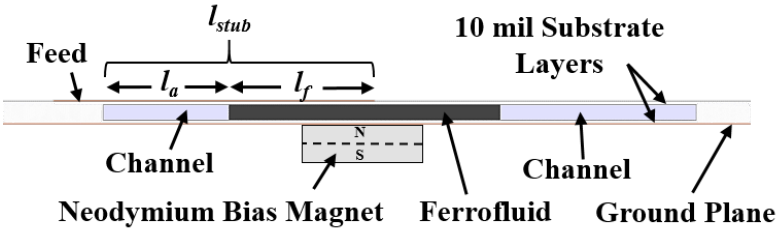

Figure 4.2: Side view of the tunable microstrip stub element. The fluid channel is "sandwiched" between two 10 mil layers of RO4350B™ due to the fabrication process. The fluid is actuated with a Neodymium bias magnet from the other side of the ground plane.

Following bonding, the 0.588 ml volume channel is filled halfway with 0.294 ml of ferrofluid and the filling hole is sealed off with a drop of epoxy. EFH1 was chosen as the loading ferrofluid because of its relatively low loss up to 2.5 GHz when under a 134 kA/m bias (Section 3.5).

A stack of five cylindrical Neodymium magnets is used to tune the microstrip stub element. Each magnet has a 12 mm diameter and 2 mm thickness, so the total stack height is 10 mm (Figure 4.3). The channel has a width of 10.7 mm, so the 12 mm diameter magnet is able to fully bias the entire width of the channel without being unnecessarily large. A cylindrical magnet has a well-characterized field, making determination of the magnet's magnetization vector from the measured strength at the magnet face a relatively straightforward task. Measurement with the A1302 sensor yielded a value of approximately 138 kA/m for a single 2 mm thick disk magnet when touching the face of the sensor to the center of the magnet. At a distance of 1.54 mm (60 mils) normal to the face of the magnet and centered on the z axis, the field strength is reduced to 106 kA/m. At the edge of the magnet normal to the face at the same distance, the measured field strength was 90 kA/m. Since the edges of the magnet overlap the edge of the ferrofluid channel, and the farthest distance to the channel along the z axis is 60 mils (see Figure 4.2), a single disk magnet applies a field strength of at least 90 kA/m to the entire channel volume normal to the face of the magnet.

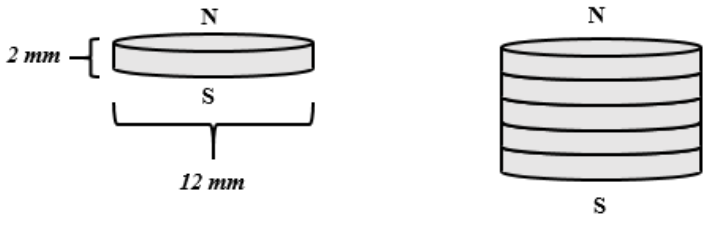

Figure 4.3: Cylindrical bias magnet dimensions and magnetic field orientation.

In order to increase the bias field strength, the cylindrical magnets can be stacked. The A1302 sensor saturates at 150 kA/m, so higher field strengths must be measured at a distance from the stack of magnets. Theoretical field strengths can also be calculated with measurement of a single magnet and solution of

$$\vec{H} = \hat{a_z}\frac{M_0}{2}\left[\frac{z}{\sqrt{z^2+b^2}} - \frac{z-L}{\sqrt{(z-L)^2+b^2}}\right], \tag{4.1}$$

for M_0, as shown in [24]. Solving (4.1) with the measurement for a single cylindrical magnet results in $M_0 = 8.55x10^5$. Thus, a stack of five cylindrical magnets has a theoretical maximum field intensity of 198 kA/m at a distance of 120 mils from the face of the stack along the z axis. When measured at a distance of 120 mils from the face, a stack of five magnets resulted in a field intensity of 149 kA/m. The measured value is lower because the discontinuities between the magnets reduce the overall field intensity [24]. At the edge, the measured intensity was 90 kA/m, and this increased to 146 kA/m at a distance of 60 mils. The theoretical field intensity at the center of the face at a distance of 60 mils is calculated to be 277 kA/m, but as shown by the results at 120 mils, the actual field intensity is roughly 25% less than its theoretical value. Therefore, the stack of five magnets has a field intensity between 146 kA/m at the edge and up to ≈ 210 kA/m at the center of its face at a distance of 60 mils. Consequently, the fluid above the magnet is biased to a field strength of greater than 134 kA/m and can be modeled with the properties in Figure 3.11.

The fluid tracks the bias magnet placement, and gravity does not have a significant influence on the fluid as confirmed with 3D printed channels with dimensions approximately equal to the channel cut into the substrate shown in Figure 4.5. The fluid leaves traces on the inner surface of the channel which could be mitigated with

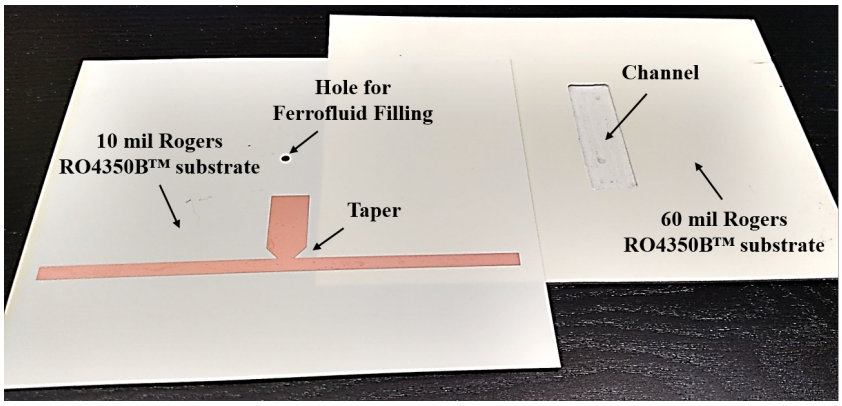

Figure 4.4: Depiction of fabricated layers. A 50 mil depth channel is milled out of the 60 mil substrate, and the microstrip design is etched onto the 10 mil substrate. The stub is aligned with the channel and the layers are bonded together with Devcon 5 Minute® epoxy. The channel is then filled halfway by volume with ferrofluid.

an oleophobic coating in future designs. This was attempted by coating the plexiglass with Tekon®B Protective Treatment, but no reduction in fluid tracing was observed. Future designs should incorporate a coating in the channel to reduce this effect - one potential solution is a "PDMS-silica nanocomposite coating" which exhibits both hydrophobic and oleophobic properties [53]. Coating the inside of the channel with this material would improve performance by reducing the loss associated with the coating of ferrofluid left on the inner faces of the channel, since this fluid layer is unbiased and therefore lossy. It would also improve predictability and repeatability, and boost the accuracy of the simple block model currently used to model the ferrofluid under bias (Section 4.2). PDMS coatings are already used in tunable microfluidic devices [17], [54].

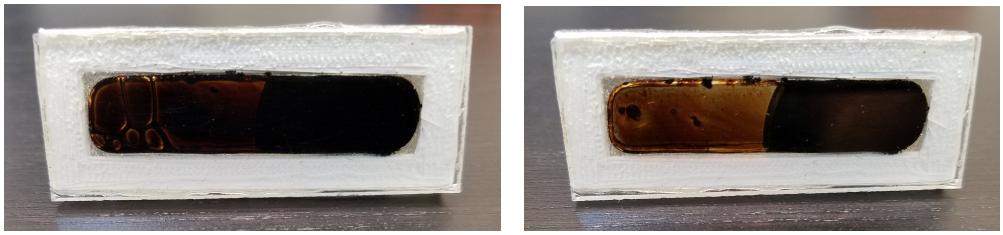

(a) (b)

Figure 4.5: 3D printed channel of approximately the same dimensions as the milled substrate channel showing fluid migration over a period of five minutes. (a) Immediately after moving the magnet to the right side of the channel, (b) Five minutes after moving the magnet to the right side of the channel.

4.2 Transmission Line Model

The circuit model of the filter element is shown in Figure 4.6. A bias magnet underneath the ground plane is used to localize the ferrofluid and move it along the length of the channel, changing the properties of the substrate beneath the stub and tuning the filter element. Due to the fluid's strong attraction to the permanent magnet, the fluid is modeled as a movable block material "sandwiched" between two 10 mil substrate layers (see Fig. 4.2). The top and bottom substrate layers are included in the calculation of the bulk properties of the substrate under the microstrip for the air and ferrofluid sections through application of the Maxwell Garnett mixing formula [55], where the two 10 mil RO4350B™ layers are approximated as inclusions in the 70 mil thick matrix medium of either air or ferrofluid (depending on the section) with a mixing ratio of $\frac{2}{7}$.

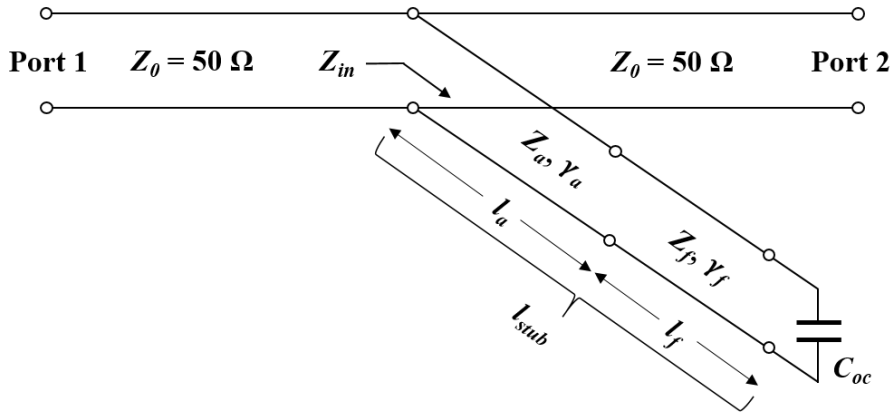

Figure 4.6: Circuit model of the stub as two series sections of transmission line loaded with a open circuit fringing capacitance C_{oc}. Modification of l_a and l_f ($l_{stub} = l_a + l_f$) models movement of the ferrofluid block.

The Maxwell Garnett formula is designed to model spherical inclusions in a matrix medium [55], but it has been found to be a good approximation of the bulk relative permittivity and permeability for the three-layer substrate in spite of the planar arrangement of the medium. An advantage of using this formula is that it approximates the effective loss of the medium as well, and is simpler and less computationally intensive than more involved methods for dealing with multilayer substrates [55]. The bulk dielectric constant of the substrate is then used to find the effective permittivity for the microstrip with formulas from [56]. The relative permeability of the fluid is close to unity, so the propagating wave will still exhibit quasi-TEM behavior as it would with a pure dielectric substrate [57]. Thus, the effective relative permeability may be easily derived from the effective relative permittivity as shown by [57] with the simple relation

$$\mu_{eff}(w/h, \mu) = \frac{1}{\epsilon_{eff}(w/h, \mu^{-1})}. \tag{4.2}$$

Microstrip impedance Z_f for the ferrofluid section is calculated using

$$Z_f = Z_c \sqrt{\frac{\mu_{eff}}{\epsilon_{eff}}} \tag{4.3}$$

from [57], where ϵ_{eff} is determined by formulas given in [56] and Z_c is the characteristic impedance for an identical microstrip with a vacuum substrate according to [56]. Propagation constants γ_a and γ_f are determined by combination of the dielectric and magnetic loss [57], and conductor loss [3] into a single attenuation constant α, which is added to wavenumber β to form the complex propagation constant $\gamma = \alpha + j\beta$ for each section of the stub. The equivalent line length l_{oc} due to the fringing capacitance C_{oc} of the microstrip is calculated with the method in [58] using the effective permittivity of the ferrofluid section. Movement of the ferrofluid is modeled by increasing the physical length of the air section l_a and decreasing the physical length of the ferrofluid section l_f by an equal amount, i.e. $l_a + l_f = l_{stub}$. As the channel is exactly twice the length of the stub, the maximum value for l_a is equal to l_{stub}. At this offset value, the substrate beneath the microstrip is entirely loaded with air, but the fringing fields at the end are still located in the ferrofluid load. Thus, l_{oc} is still calculated with the effective permittivity of the ferrofluid substrate even at maximum bias offset. This is an approximation, as the method given by [58] assumes a homogeneous substrate around the microstrip discontinuity; thus, the accuracy of the determined l_{oc} will be highest in the middle of the tunable range, since the microstrip and the fringing fields will be nearly entirely contained within the ferrofluid-loaded substrate.

The air-loaded substrate section of the stub is modeled as

$$ABCD_a = \begin{bmatrix} \cosh(\gamma_a l_a) & Z_a \sinh(\gamma_a l_a) \\ \frac{1}{Z_a}\sinh(\gamma_a l_a) & \cosh(\gamma_a l_a) \end{bmatrix}, \tag{4.4}$$

and the ferrofluid-loaded section is modeled as

$$ABCD_f = \begin{bmatrix} \cosh(\gamma_f (l_f + l_{oc})) & Z_f \sinh(\gamma_f (l_f + l_{oc})) \\ \frac{1}{Z_f}\sinh(\gamma_f (l_f + l_{oc})) & \cosh(\gamma_f (l_f + l_{oc})) \end{bmatrix} \tag{4.5}$$

which is a standard representation of a lossy transmission line in [3]. The sections are combined into a single matrix by multiplying to represent the cascade where $ABCD_{stub} = ABCD_a * ABCD_f$, which represents the transmission line characteristics for the entire stub loaded with the fringing capacitance. From standard network theory in [3], $ABCD$ parameters can be used to find the input impedance, Z_{in}, for a loaded 2-port network, which simplifies to

$$Z_{in} = \frac{ABCD_{stub}(1,1)}{ABCD_{stub}(2,1)} \tag{4.6}$$

for an open circuit end load impedance [3]. The overall system response of the two port network is determined by centering the shunt input admittance $\frac{1}{Z_{in}}$ between the 50 Ω feed lines connecting the stub to the ports.

4.3 Results

As shown by Figures 4.7, the filter with the reconfigurable stub element has a measured tunable range of 640 MHz, resulting in a fractional tunable bandwidth of 29%. Figure 4.7 shows that measured attenuation in the stopband remains below -30 dB

for the entire tunable range. One notable result is that a bias magnet offset of 5 mm actually results in a lower tuned frequency than an offset of 0 mm (Figure 4.7). This is likely due to the bias magnet's diameter being less than the length of the fluid block, resulting in uncertainty in the spatial distribution of the fluid in the channel as the bias magnet nears the channel ends. At the channel ends, the bias field will not be centered on the fluid, potentially changing the shape of the fluid and reducing the accuracy of the "block" model. Thus, there is a degree of uncertainty in the exact value of l_a for the measured data due because the bias magnet diameter is 12 mm while the stub length is 21.67 mm; however, the trend of operating frequency increasing with bias magnet offset is readily apparent and repeatable. Another potential explanation is that the volume of fluid actually filled is not exactly half of the channel volume, and is in fact slightly less. This would load the stub more at a small offset than at zero offset, since the fringing fields would be loaded with fluid at a slight offset but loaded with air at zero offset. Antenna designs presented in Chapter 5 and 6 implementing this tuning method incorporate fluid channels with a length greater than twice the stub length in order to allow for some tolerance in the volume of fluid filled, and improve fluid-placement predictability.

A comparison between the transmission line model, simulation in HFSS [59], and measurement at the ends of the tunable range is shown in Figure 4.8. The calculated and simulated results use the measured properties of EFH1 under the maximum bias (Figure 3.11). The transmission line model exhibits a frequency shift in the predicted insertion loss at the high end of the tuning range (Figure 4.8(a)), which is most likely due to a higher-order electromagnetic effect that the model is unable to capture. The shift indicates that the transmission line model is less accurate when predicting the loading effects of the air-filled section of the stub, potentially meaning that the Maxwell-Garnett approximation is not as accurate for

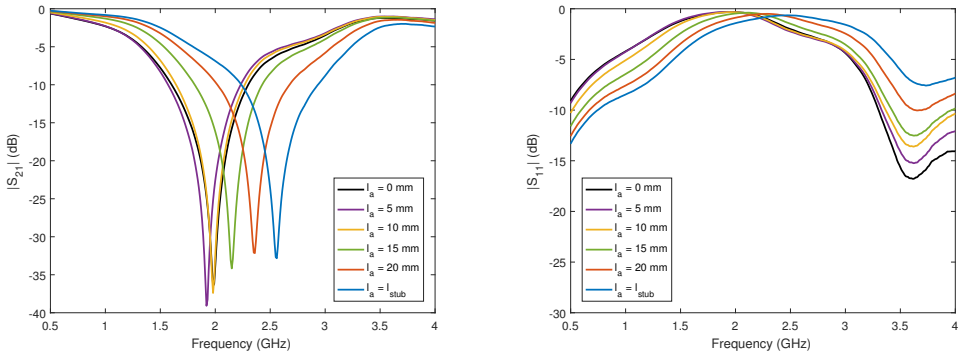

(a) (b)

Figure 4.7: Measurement of the microstrip stub filter element as the bias magnet edge is placed at 5 mm increments from the stub attachment point: (a) Insertion loss, (b) Return loss. The stub has a tunable fractional bandwidth of 29%.

the air section as it is for the ferrofluid section. This behavior is not unexpected, as air exhibits a much greater difference in permittivity from Rogers RO4350B™ substrate than EFH1. The transmission line model also predicts significantly lower insertion loss at the high end of the tunable range, which could be due to the model not completely capturing the loss associated with the fringing fields at the end of the stub. Overall, strong agreement is seen between the transmission line model, simulation, and measurements.

4.3.1 Tuning at a Distance

In order to tune the stub element at a distance, an external magnetic bias field is applied. Figure 4.10 shows the back side of the filter element with a stack of five cylindrical Neodymium disk magnets sitting behind the ferrofluid. The bias magnets are attracted to the ferrofluid, and remain in place regardless of the orientation of the stub. Repositioning the magnets moves the fluid beneath the stub, which tunes frequency response of the filter element. The magnets can be repositioned by

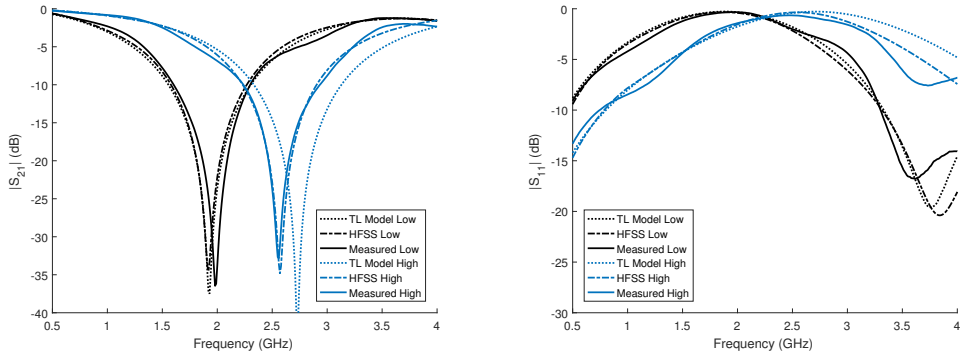

(a) (b)

Figure 4.8: Comparison of the calculated, simulated, and measured filter element response at the ends of the tunable range (l_a = 0 mm and $l_a = l_{stub}$): (a) Insertion loss, (b) Return loss. The transmission line model exhibits a slight frequency shift from the measured and simulated results at the high end of the tunable range.

directly moving the magnets if the ground plane of the device is accessible. Otherwise, they can be repositioned at a distance with the assistance of a 3D printed plastic structure to align the permanent bias magnets along the channel as shown in Figure 4.11, and an external biasing field (which in its simplest form may be another permanent magnet). Figure 4.9 shows a cross-sectional view of the setup.

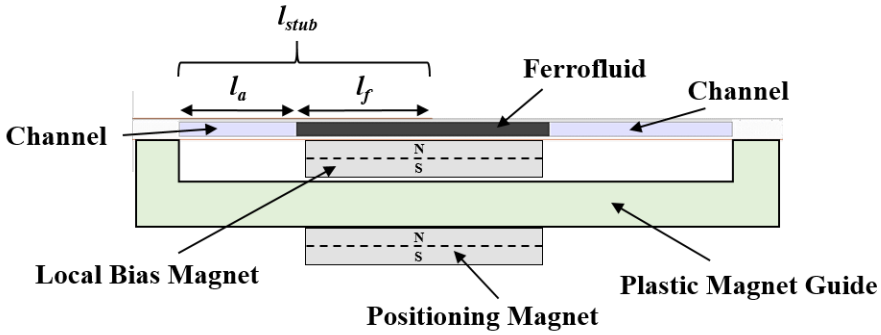

Figure 4.9: Diagram of repositionable ferrofluid load. Upon application of an external positioning field, the local bias is pulled away from the fluid such that it can move along the length of the plastic guide. After removal of the positioning field, the local magnet is again attracted to the fluid, and remains in place due to the attraction between the magnet and the fluid.

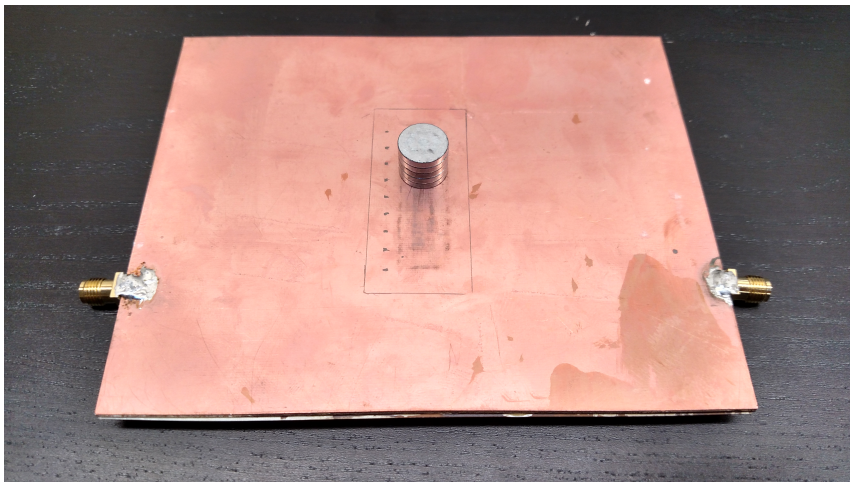

Figure 4.10: Uncovered tunable stub element ground plane showing permanent bias magnets in place. The stub is tunable through manual movement of the magnets if the ground plane is physically accessible.

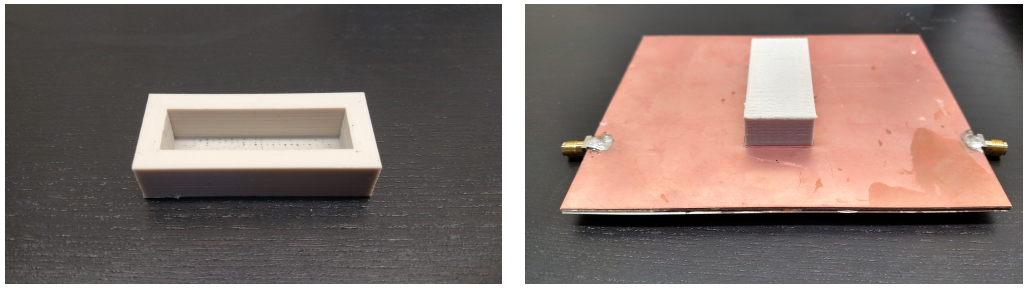

(a) (b)

Figure 4.11: 3D printed permanent magnet guide: (a) Upside down view, (b) After covering the local bias magnets. Securing the plastic magnet guide to the ground plane allows for tuning at a distance through application of an external positioning field to lift the internal magnets and move them. This is possible at distances up to 28 mm away from the container edge.

4.3.2 Repeatability of Tuning

EFH1 exhibits an attractive force to a magnetic bias, which increases the friction between the bias magnet and the ground plane. This friction is what makes the system resistant to detuning due to gravity or movement. As long as the system does not experience an excessive amount of force, a stack of five cylindrical bias magnets is sufficient to remain in place regardless of orientation of the device. Figure 4.12 demonstrates a comparison of the filter element's response at different orientations. As the data shows, the magnetic bias field is strong enough to oppose the effects of gravity such that fluid remains localized around the bias. When the stub is oriented such that gravity causes the fluid to flow out from underneath, the response is identical to the stub biased in the same configuration and oriented such that gravity exerts a force opposing the fluid placement.

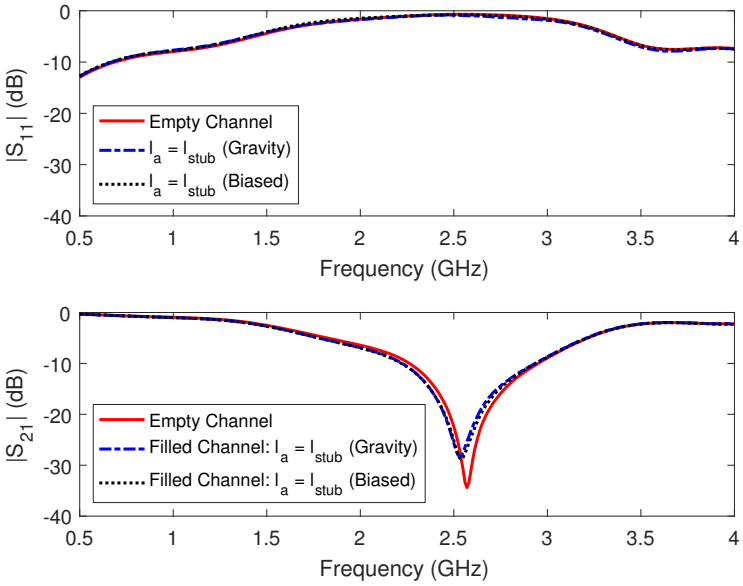

Figure 4.12: Comparison of stub response with and without a magnetic bias field at different orientations. No change in insertion loss is noticeable for different orientations of the device.

In order to test how well device remains tuned to a specific frequency, the stub was tuned to a frequency of 2.05 GHz and left configured for a period of three weeks. The orientation was changed occasionally as well to test the effect of gravity. The response was measured and recorded periodically, and results are shown in Figure 4.13. The insertion loss null demonstrates a variation of approximately 30 MHz and 4 dB over time. As shown in Figure 4.13(b), the null has a slightly lower value with each measurement, which could be explained by migration of the thin layer of fluid left coating the inside of the channel after the initial tuning, such as seen in Figure 4.5. Some of this variation may be attributable to measurement error as well.

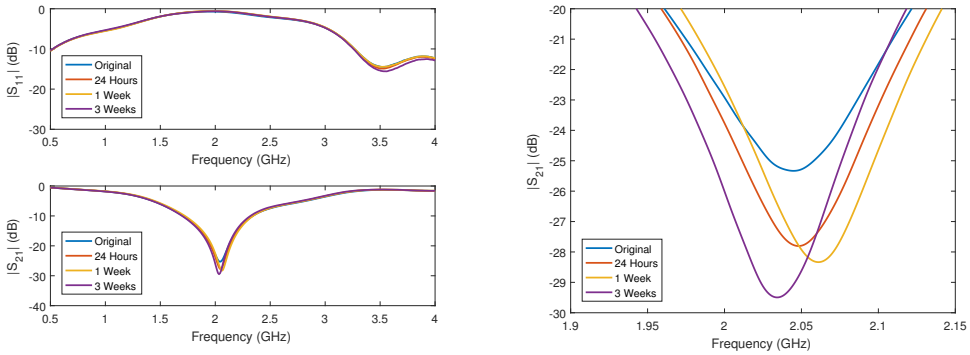

(a) (b)

Figure 4.13: Variation in the insertion loss of the tunable stub element biased for an extended period of time and measured periodically: (a) Wideband response, (b) Close-up of the insertion loss null. A slight variation in tuned frequency over time is noticeable, and could be due to migration of a thin layer of fluid coating the channel.

One important consideration is the effect of a bias field remaining applied to the fluid for an extended period of time. According to [40], magnetite-based ferrofluids biased at a field strength of 90 kA/m have an upper limit on the stable particle diameter of 5.3 nm. As EFH1 has a nominal particle size of 10 nm and the bias field strengths used are in the range of 146 kA/m and higher, the particles may tend to agglomerate over a long period time. Thus, further work must be done to test ferrofluid stability over time, and device tuning repeatability and longevity.

4.4 Conclusions

The input impedance to microstrip stub element can be tuned by repositioning a ferrofluid loaded in a channel in the substrate. The geometry of a microstrip line ensures that the electric fields largely remain in the substrate between the strip and the ground plane, so loading this volume with a movable load like ferrofluid has a significant impact on the overall electromagnetic behavior of the stub. Movement

of the fluid changes the relative filling fractions of air and fluid in the substrate volume, resulting in a tuning effect on the input impedance of the stub. The tunable microstrip element is easily loaded onto planar devices like microstrip filters and patch and slot antennas, and ensures electrical isolation between the RF system and the tuning system. Compared to conventional ferrite tuning methods, ferrofluid actuation is superior in that it can be done at a distance, and solely with permanent magnets. Ferrites exhibit a continuous change in permeability as the bias field strength is changed, but a continuous change in bias field strength requires coils and a controlled current source, significantly increasing the power draw and complexity of the system. Tuning through repositioning of permanent magnets, on the other hand, only requires an external field when repositioning the magnets, and thus requires much less power. Future designs utilizing this loading element are expedited by development of a computationally efficient transmission line model that shows strong agreement with measured and simulated results up to a frequency of 3 GHz.

Chapter 5

Reconfigurable Patch Antenna Using Repositionable Ferrofluid Loads

This chapter demonstrates several patch antenna designs utilizing variants of the tunable microstrip stub presented in Chapter 4. Two variants of a stub-loaded patch antenna are designed and tested, along with an improved patch antenna designed to overcome the limitations of the first two versions. In addition to symmetric tuning, the improved patch antenna is covered with two different superstrates, and compensation for the loading of the superstrates is demonstrated through asymmetric tuning of the stubs. The antennas are designed to be tunable across both frequency and input impedance, making them adaptable to a large range of applications. Stub-loaded patch antenna design ideas are proposed by [60]–[62]. Many of these designs are focused on using the stubs to generate dual band operation of the patch antenna with monolithic stubs, indicating that loading a patch antenna with microstrip stubs has an impact on the operating frequency of the antenna. This is the impetus for a stub-loaded patch antenna (Figure 5.1) based on the tunable microstrip element presented in Chapter 4.

The first patch antenna design using the candidate loading structure is a patch antenna loaded at each end with a single tunable stub. This symmetric layout al-

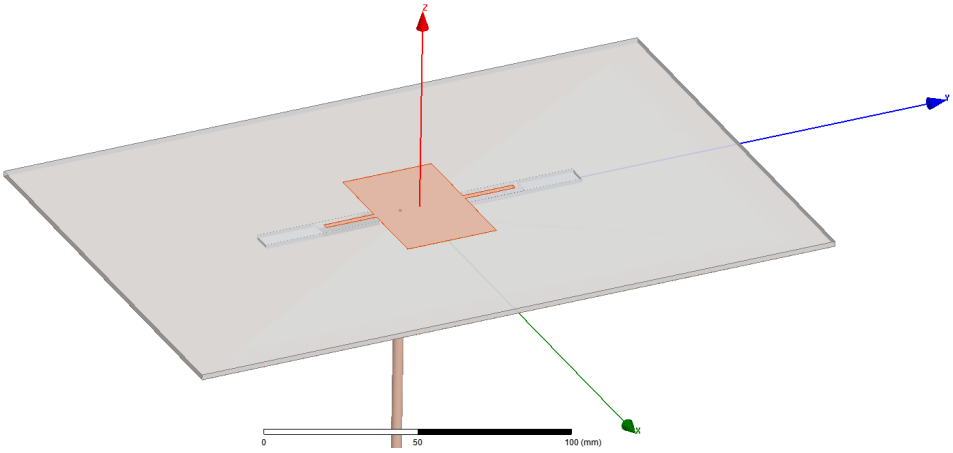

Figure 5.1: HFSS model of the stub-loaded patch antenna design. The coaxial probe feed point is inset 9 mm from the left edge of the patch. Each stub has a width of 2 mm and a length of 18 mm.

lows for both frequency and impedance tunability. The second design is loaded with three stubs at each end of the patch in an attempt to improve the tunable bandwidth, but measured results show low efficiency and unpredictable performance. The improved design utilizes smaller fluid channels than the first two designs in order to reduce fluid loss, and offsets the channel edges from the patch edge by a small distance to reduce interaction between the radiating fields and the ferrofluid.

5.1 Transmission Line Model

Operation of the patch antenna is modeled by adding the stub input admittance $Y_l = \frac{1}{Z_{in}}$ from the tunable stub model in Figure 4.6 to each slot admittance Y_s in Pues and Van de Capelle's patch antenna transmission line model (Figure 5.2) [63]. Load admittances Y_{l1} and Y_{l2} represent the stub input admittances at the edges of the patch. The stubs can be tuned independently, so Y_{l1} is equal to Y_{l2} only during symmetric tuning of the stubs. The stub width has a reducing effect on the radiating

slot admittance Y_s, which is accounted for by the ratio

$$r = 1 - \frac{W_m}{W_e}, \tag{5.1}$$

where W_m is the width of the stub and W_e is the effective width of the patch antenna as suggested by [63]. For cases where the patch is loaded with multiple stubs at each end, W_m is simply multiplied by the number of stubs; e.g., the patch loaded with three stubs of width 2 mm each will have $W_m = 6$ mm (Section 5.3). This is an approximation, and its accuracy is reduced as the number of stubs is increased, as effects like coupling between the loading stubs will become more pronounced.

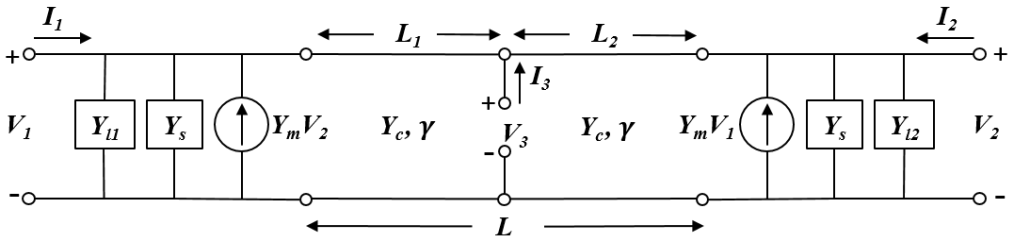

Figure 5.2: Pues and Van de Capelle's transmission line model for a rectangular patch antenna [63] modified to include the stub input admittances Y_{l1} and Y_{l2} loaded at each end of the patch.

According to Pues and Van de Capelle [63], the input admittance to an unloaded rectangular patch antenna probe-fed at V_3 (see Figure 5.2) is

$$Y_{in} = 2Y_c * \left[\frac{{Y_c}^2 + {Y_s}^2 - {Y_m}^2 + 2Y_s Y_c \coth(\gamma L) - 2Y_m Y_c \operatorname{csch}(\gamma L)}{({Y_c}^2 + {Y_s}^2 - {Y_m}^2)\coth(\gamma L) + ({Y_c}^2 - {Y_s}^2 + {Y_m}^2)\cosh(2\gamma\Delta)\operatorname{csch}(\gamma L) + 2Y_s Y_c} \right] \tag{5.2}$$

where

$$\Delta = \left| \frac{L}{2} - L_1 \right| = \left| \frac{L}{2} - (L - L_1) \right| \tag{5.3}$$

and L_1 is the offset distance of the feed from the patch [63]. Y_c and γ are the characteristic admittance and propagation constant of the patch, L is the length of the patch, and Y_m is the mutual admittance between the radiating fields at the ends of the patch [63]. Loading the patch antenna with stubs effectively changes the admittance of the radiating slot, Y_s, so the stub input admittances Y_{l1} and Y_{l2} are added to Y_s in (5.2) to account for the loading of the stubs. Return loss in dB is defined as

$$\mathrm{RL} = -20\log_{10}|\Gamma| \tag{5.4}$$

where

$$\Gamma = \frac{1 - Z_0 Y_{in}}{1 + Z_0 Y_{in}} \tag{5.5}$$

for a reference impedance Z_0 and the antenna input admittance Y_{in} defined in (5.2) [3]. The optimization process calculates the tuning range by finding the tunable fractional bandwidth with the formula

$$\mathrm{BW} = \frac{f_h - f_l}{\sqrt{f_h f_l}} \tag{5.6}$$

where f_h is determined by the highest tunable frequency and f_l is determined by the lowest tunable frequency. In order to optimize the tunable range of the antenna, a simple optimization algorithm based on the transmission line model is carried out in MATLAB®. The algorithm optimizes the stub lengths and widths and the width of the patch in order to maximize the tunable fractional bandwidth, where f_h and f_l are required to have RL values of 10 dB or greater as determined by (5.4).

5.2 Patch Antenna End-Loaded with Single Stub

5.2.1 Design

In order to ensure operation in a frequency range where fluid loss is low, the patch antenna is designed to have a tunable range below 2.5 GHz. Thus, the optimization process was constrained to a patch length of at least 32 mm. The algorithm returned dimensions for the patch of $W = 50$ mm and $L = 32$ mm, and the stubs were optimized to have a width of 2 mm and a length of 18 mm (see Fig. 5.1). In contrast to the stub loading element design in Chapter 4, the channel width must be larger than the width of the stubs in order to more completely capture the electric fields, because the smaller stub width results in a smaller effective permittivity, which reduces the effective filling factor of the fields

$$q = \frac{\epsilon_{eff} - 1}{\epsilon_r - 1}, \tag{5.7}$$

according to [64]. As shown by an HFSS simulation of the antenna loaded with 2 mm wide stubs over a varying channel width (Figure 5.14), negligible impact is noticed on the tunable bandwidth as long as the channel width is kept above 4 mm. In order to retain as much bandwidth as possible, the channel width was chosen to be 7.3 mm.

Some pictures of the patch antenna fabrication process are shown in Figure 5.3. Fabrication of the antenna is done in a similar manner to the process outlined in Section 4.1. The antenna is fabricated using two RO4350B™ substrates of 60 mil and 10 mil thickness. The patch design is etched on the top layer, and the channel outlines and the feed location are etched onto the bottom layer. The bottom layer channel outlines are milled out, as shown in Figure 5.3(b), and a hole is drilled through the substrate at the feed point. The channels are milled to a nominal depth of 50 mils.

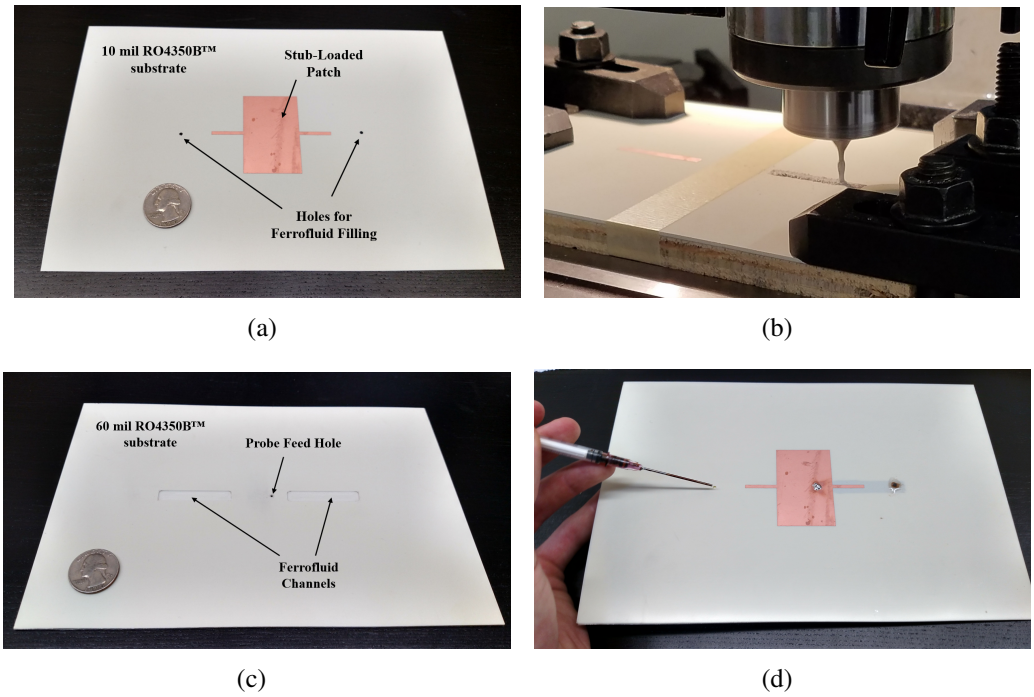

Figure 5.3: Fabrication pictures of the single stub-loaded patch antenna: (a) 10 mil substrate layer with antenna design, (b) Milling of the 60 mil bottom substrate layer, (c) Bottom substrate layer after channel milling, (d) Filling of the channels with a syringe.

The two layers are then aligned, and bonded together with a thin layer of Devcon 5 Minute® epoxy. After the epoxy is cured, the feed hole is drilled through the top layer, and the SMA connector is soldered to the patch and the ground plane. Finally, the channels are each filled halfway by volume with EFH1 ferrofluid, and sealed with a drop of epoxy. In order to reduce the uncertainty of fluid placement near the channel ends, the channels are designed to have a length 5 mm longer than the stub length, and the fluid is filled to a volume such that it extends 2.5 mm past the stub end at zero offset placement (Figure 5.4(a)). Extension of the channel length beyond twice the stub length results in a larger tunable range because the fluid loads the fringing fields when $l_a = 0$ mm, and the fringing fields are unloaded when the fluid is at the maximum offset distance (Figure 5.4(b)).

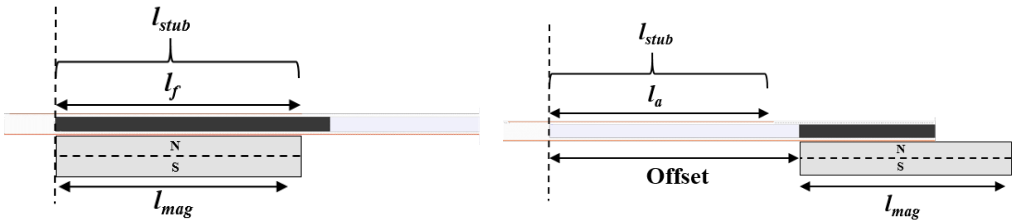

(a) (b)

Figure 5.4: Cross-sectional diagram of fluid placement: (a) At minimum offset, (b) At maximum offset. Increasing the channel length ensures that the fluid loads the stub's fringing fields at minimum offset, and does not load the fringing fields at maximum offset.

5.2.2 Results

The measured tunable frequency range of the antenna is shown in Figure 5.5(a), and a comparison of calculated, simulated, and measured values at the high and low ends of the tunable range is shown in Figure 5.5(b). As with the isolated microstrip element presented in Chapter 4, the 'mm' offset values in the legend correspond to

the measured offset distance of edge of the bias magnet from the end of the channel closest to the stub attachment point. The measured tunable bandwidth of 9.9% is marginally lower than the simulated bandwidth of 14.8%. The ferrofluid channels were milled to a nominal depth of 50 mils, but the results show that the channel depth was less than 50 mils in reality. This reduced channel depth was attributed to human error during manual milling of the channel. A reduction in channel depth explains the reduced ability to tune to higher frequencies because the air pocket formed underneath the stub has less effect on the bulk substrate properties in the channel. Measurements agree relatively well with the simulation at the low end of the tunable range even with a reduced channel depth because the ferrofluid has a dielectric constant close to that of the substrate.

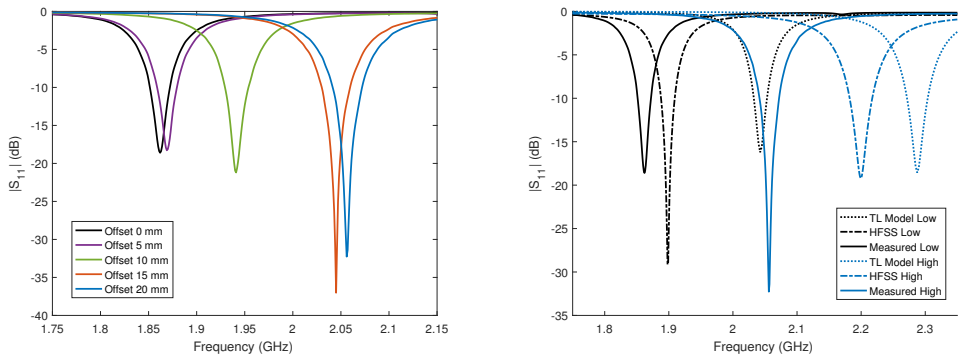

(a) (b)

Figure 5.5: Single-stub patch antenna return loss at various bias magnet offset placements as the stubs are tuned symmetrically: (a) Measured return loss at several offsets, (b) Comparison of calculated, simulated, and measured return loss of the patch antenna at the end points of the tunable range. The measured tunable fractional bandwidth is 9.9%.

Figure 5.6 shows a mismatch between the E-plane and H-plane measurements of realized gain at broadside. This is likely due to the changing orientation of the antenna during testing (see Figure 5.7). When measuring the H-plane, the stubs are aligned such that any unbiased fluid under the effect of gravity will only load the

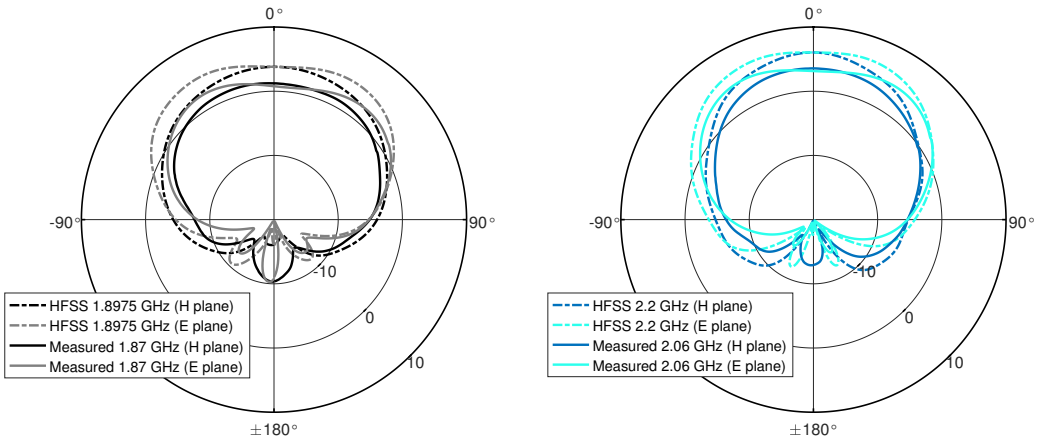

(a) (b)

Figure 5.6: Comparison of realized gain measurements and simulations in the E-plane and H-plane: (a) Realized gain at the lowest tunable frequency, (b) Realized gain at the highest tunable frequency.

end of one of the stubs. During E-plane measurements, the sideways orientation of the antenna increases the likelihood that any unbiased fluid will affect the ends of both stubs, reducing the efficiency at this orientation because unbiased fluid exhibits a much higher magnetic loss tangent. Furthermore, Figure 5.6 demonstrates measured realized gain at broadside of up to 3 dB less than simulated. This discrepancy is likely due to incomplete biasing of the ferrofluid in the channels, which results in a higher loss tangent for the fluid and lowered antenna efficiency. This effect was investigated further with the improved patch antenna design in Section 5.4. Simulation of a thin layer of unbiased ferrofluid coating the channel results in a reduction in gain on the order of 2 dB, which helps to explain the lower measured gain of the patch.

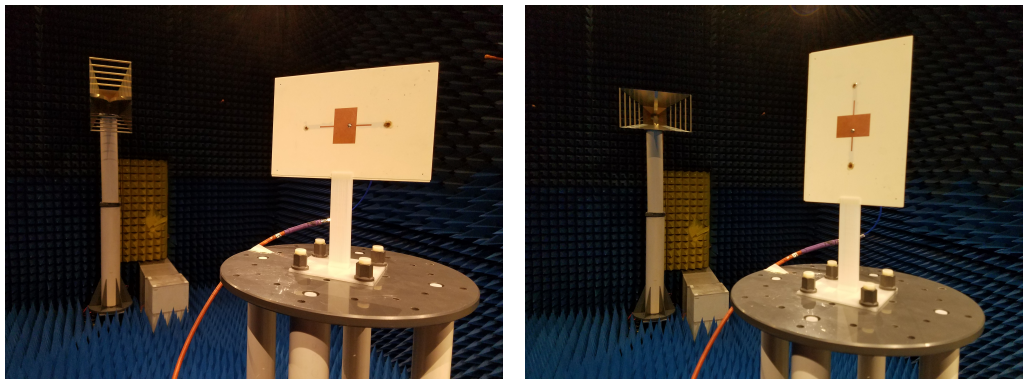

(a) (b)

Figure 5.7: Pictures of antenna orientation during E-plane and H-plane measurements: (a) E-plane orientation, (b) H-plane orientation. Antenna orientation may have an effect on any unbiased fluid remaining in the channel. E-plane measurements are more likely to suffer from reduced gain if the channels contain unbiased fluid because both stubs will be affected.

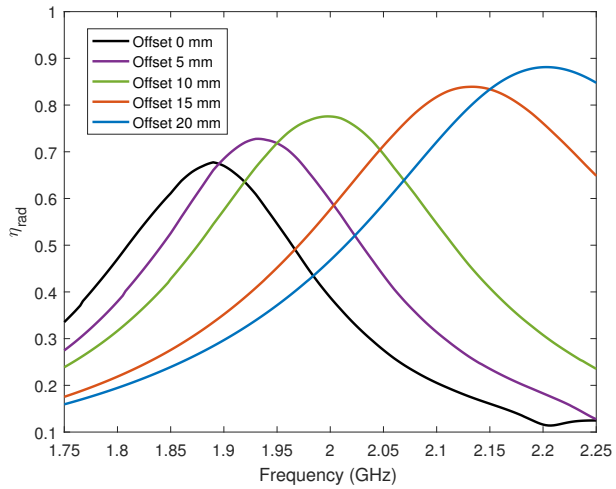

Figure 5.8: Radiation efficiency for the one stub version of the patch during symmetric tuning. Simulated efficiency is above 65% for the entire tunable range, and increases marginally as a function of tuned frequency.

5.3 Patch Antenna End-Loaded with Three Stubs

5.3.1 Design

The patch antenna may also be loaded with multiple stubs at each end. An antenna was designed with three stubs loading each end of the patch (Figure 5.9). The stubs are spaced by $\frac{1}{3}$ of the patch width, as suggested by the authors of [9]. The same optimization procedure was carried out as with the single stub version of the patch, the only difference being that W_m (5.1) was multiplied by three in order to account for the increased number of stubs. Computations with the transmission line model and simulation in HFSS of this version show an improvement on the tunable fractional bandwidth of the single stub antenna. However, real world biasing of the increased amount of fluid requires a much larger and stronger biasing field. The width of the fluid channel must be increased to the 49 mm width of the patch in order to properly load all of the stubs. This results in an increase in fluid volume up to 1.08 cc when the 50 mil channel is filled such that fluid reaches out to the end of the stubs. In practice, as with the first fabrication of the single stub patch, the channels did not reach a depth of 50 mil but were actually closer to 35 mil on average. Nevertheless, the fluid volume was still 0.76 cc which was significantly more fluid than required for the single stub version (0.12 cc).

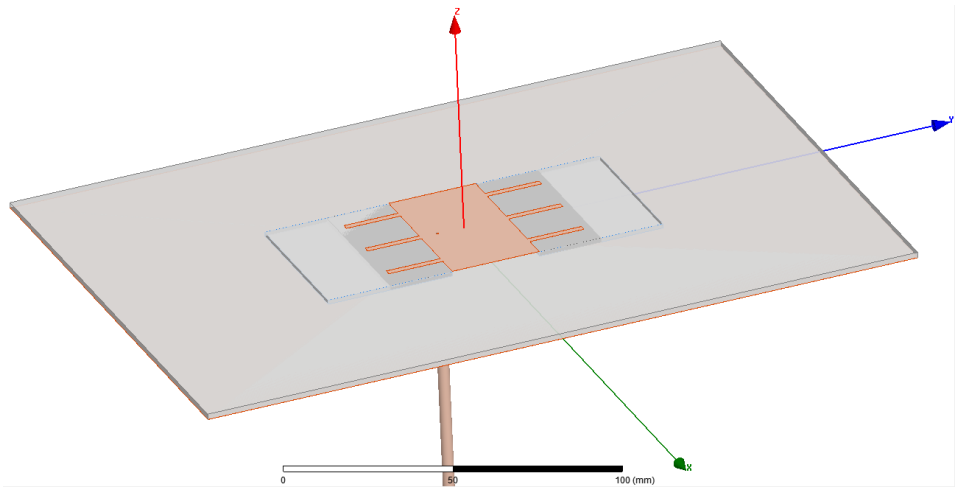

Figure 5.9: Model of patch antenna loaded with three stubs at each end. Each stub is 2 mm wide and 17.4 mm long. The coaxial feed point is inset 5.5 mm from patch edge.

5.3.2 Results

The antenna was tuned with two large bar magnets with dimensions of 3 x 0.5 x 0.25 inches. Even though the bias magnet width of 12.7 mm was not as wide as the 19.9 mm long fluid block, the bias magnet fields were strong enough to interfere with each other, making biasing to lower offsets difficult. Depending on their orientation, the magnets either attracted or repulsed each other when the antenna was symmetrically tuned to offset values of 10 mm or lower.

Figure 5.10(a) shows the measured return loss of the antenna as the stubs are tuned symmetrically. Measurements show that performance of the three stub patch antenna is much less predictable than the single stub design. Figure 5.10(b) shows a comparison of the calculated, simulated, and measured return loss at the low and high ends of the tunable range. Both simulation in HFSS and the transmission line model of the antenna predict a much larger tuning range than measured. The measured tunable fractional bandwidth is only 3.4%, compared to a simulated fractional bandwidth of 25.9%. The discrepancy here is likely due to several factors: Since the

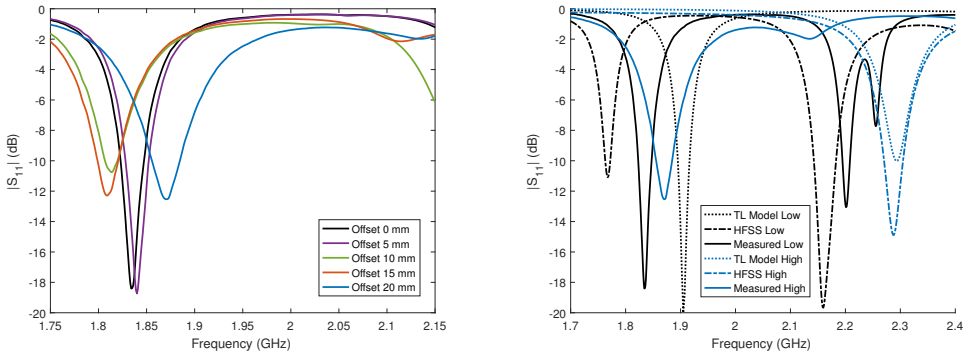

(a) (b)

Figure 5.10: Three-stub patch antenna return loss at various bias magnet offset placements as the stubs are tuned symmetrically: (a) Measured return loss at several offsets, (b) Comparison of calculated, simulated, and measured return loss of the patch antenna at the end points of the tunable range. The three stub version has a lower measured tunable bandwidth of 3.4%, and is less predictable.

ferrofluid channel is the entire width of the patch, at low offset values the fluid significantly loads the fringing fields along the entire width of the patch, changing the distribution of the radiating fringing fields along the patch edges. Furthermore, the large amount of fluid likely results in incomplete biasing by the permanent magnetic field, increasing the fluid loss and reducing the efficiency of the antenna. Finally, the interference between the biasing fields occurring at small offsets likely results in unpredictable fluid distributions. Performance could potentially be improved by dedicating individual channels to each stub, but this also would increase the difficulty of fabrication, and each channel would likely be filled with a slightly different volume of fluid, resulting in unpredictability. Furthermore, even with individual channels, large bias fields would still be required to actuate the fluid, resulting in either attraction or repulsion between the bias fields and difficulty in tuning to configurations where the fluid offset is low.

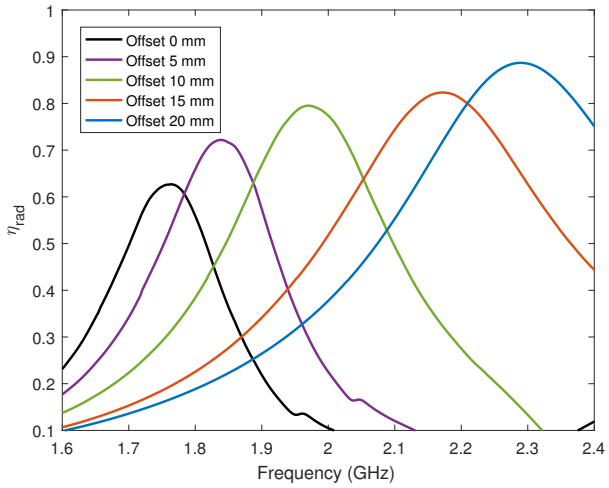

Figure 5.11: Radiation efficiency computed by HFSS. Efficiency values are comparable to the single stub case (Figure 5.8).

5.4 Improved End-Loaded Patch Antenna

5.4.1 Design

Reduction in ferrofluid volume is desirable, since as determined in Section 3.3, even under a strong permanent magnetic bias, EFH1 exhibits a non-negligible loss tangent of up to 0.05 below 2.5 GHz, which is more than an order of magnitude greater than the loss tangent of Rogers RO4350B™ ($\tan\delta_e = 0.0031$). Additionally, reduction in fluid volume reduces the mass of the fluid and facilitates easier movement with the biasing field and improved tracking of the bias magnet. Reduction in fluid volume helps to avoid the issues experienced with the original design where the orientation slightly changed the realized gain of the antenna at broadside (Figure 5.6), and the unpredictable fluid placement exhibited by the three stub patch antenna (Section 5.3.2). The first version of the single stub loaded patch antenna was designed with 7.3 mm wide channels. According to a parametric simulation run in HFSS, the channel width can be reduced down to 4 mm before the tuning

range is severely impacted (Figure 5.14). Thus, the channel width was reduced to 5 mm in order to reduce the amount of required fluid and the effect of gravity on fluid placement. In addition, the fluid channels were offset from the patch edge by a distance $l_s = 1.5$ mm to avoid interference with the patch's radiating fringing fields (Figure 5.15). The patch has a radiating slot of width 1.03 mm according to [58], so offsetting the fluid channels by 1.5 mm from the patch edge significantly reduces the interaction between the ferrofluid and the radiating fields. An additional matrix, $ABCD_s$, is required to account for the section of microstrip line with length l_s in the stub's transmission line model (Figure 4.6).

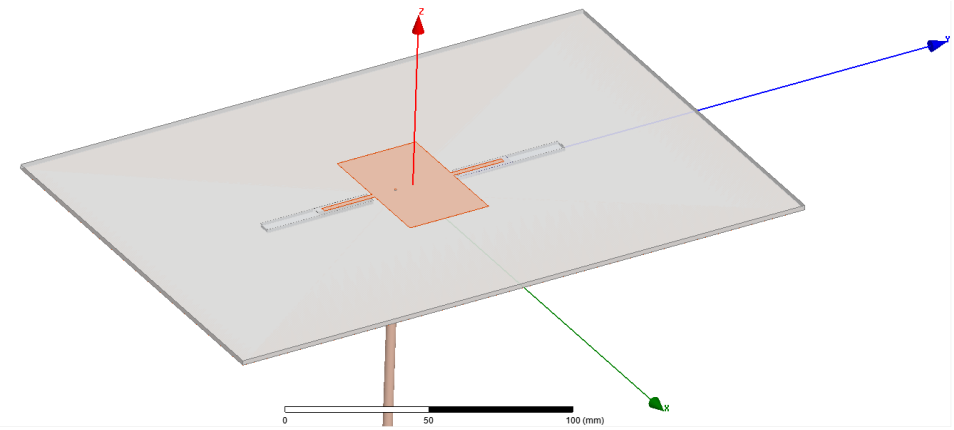

Figure 5.12: Improved patch antenna design. The coaxial feed point is inset 9 mm from the patch edge ($L_1 = 9$ mm). Each stub is 2 mm wide and 19 mm long. The fluid channel width is reduced to 5 mm, and is placed 1.5 mm from the patch edge in order to avoid interference with the patch's fringing fields.

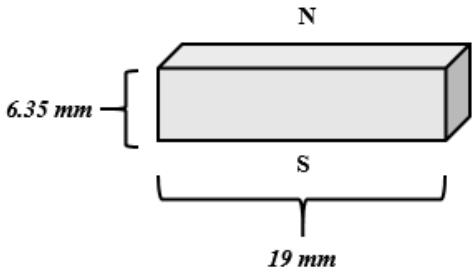

Figure 5.13: Rectangular bias magnet dimensions and magnetic field orientation.

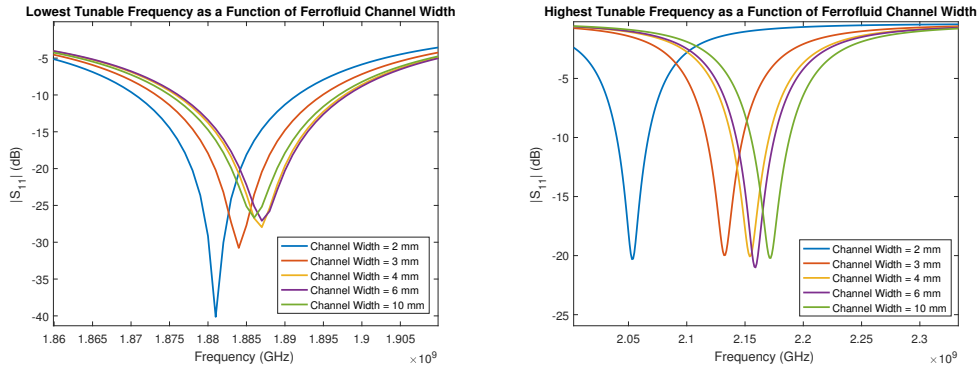

(a) (b)

Figure 5.14: Comparison of simulated single stub patch antenna return loss as the fluid channel width is changed: (a) At the lowest tunable frequency, (b) At the highest tunable frequency.

The fluid is biased with a rectangular magnet with dimensions of 6.35 x 6.35 x 19 mm. The rectangular magnet's measured field intensity at a distance of 120 mils from the center of its face was 137 kA/m. At the edge, the field strength dropped to 105 kA/m. At a distance of 60 mils from the face, the sensor saturated at the center, and measured a field strength of 149 kA/m at the edge. The measurements are similar to what was measured for the stack of cylindrical magnets, in that across the entire face at a distance of 60 mils, the field intensity is greater than 146 kA/m.

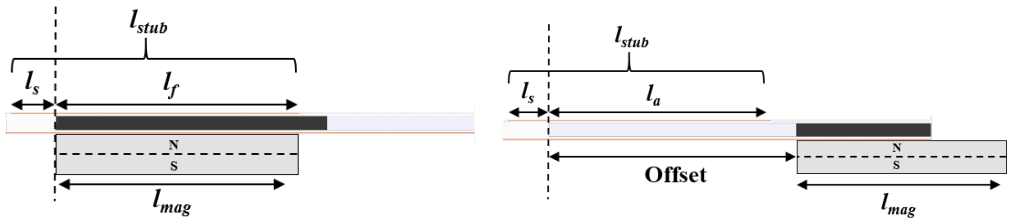

(a) (b)

Figure 5.15: Cross-sectional diagram of fluid placement: (a) At minimum offset, (b) At maximum offset. Increasing the channel length ensures that the fluid loads the stub's fringing fields at minimum offset, and does not load the fringing fields at maximum offset.

5.4.2 Results

Symmetric Tuning

The improved patch antenna design performs much closer to simulation. As shown by Figure 5.16, the measured fractional bandwidth is 16.6%, which is nearly equal to the simulated bandwidth of 17.7%. Furthermore, the lowest measured operating frequency is only 10 MHz lower than simulated, and the highest tunable frequency is 30 MHz lower. The transmission line model still shows a frequency shift with the improved design, though the predicted fractional bandwidth of 15.4% is approximately equal to the measured and simulated values, meaning that the model is useful for predicting the tunable bandwidth. Figure 5.17 shows that the measured realized gain increases slightly as the antenna is tuned higher in frequency, and cross-pol isolation is greater than 20 dB at broadside for both measured cut planes.

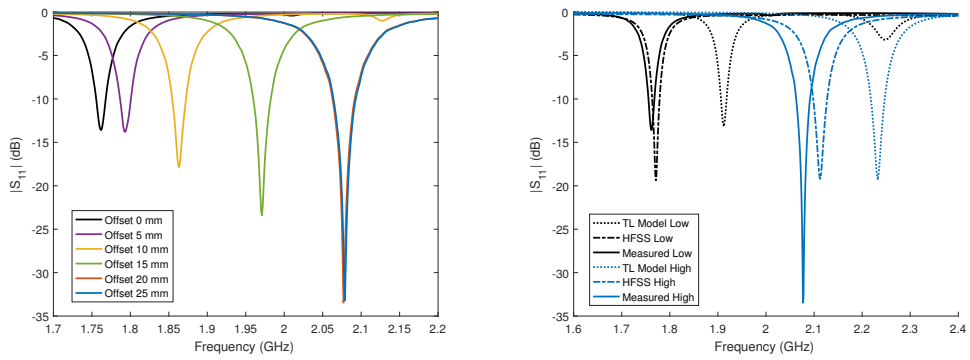

(a) (b)

Figure 5.16: Improved patch antenna return loss at various bias magnet offset placements as the stubs are tuned symmetrically: (a) Measured return loss at several offsets, (b) Comparison of calculated, simulated, and measured return loss of the patch antenna at the end points of the tunable range. The improved patch antenna design has a measured fractional bandwidth of 16.6%, and shows the strongest agreement between measurement and simulation out of the three tested patch designs.

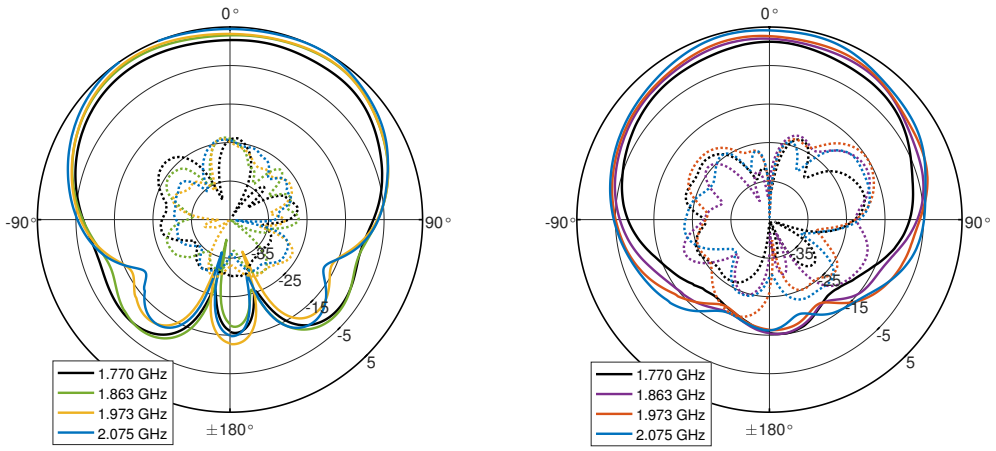

(a) (b)

Figure 5.17: Measurement of realized gain in the E-plane and H-plane at several tuned frequencies: (a) E-plane, (b) H-plane. The solid traces are co-polarized patterns, and the dotted traces are measurements of the cross-polarization. The cross-pol isolation is greater than 20 dB at broadside in both measured planes.

Figure 5.18 shows a comparison between the simulated and measured realized gain at the lowest and highest tunable frequencies. The measured pattern shape is very similar to the simulated shape, and is roughly 1.5 - 3 dB lower than simulated. Simulated radiation efficiency of the improved patch design (Figure 5.19) shows comparable values to the efficiency simulated for the previous single stub design (Figure 5.8), though roughly 10% lower at the lowest tunable frequency. Further optimization of the patch dimensions could potentially improve the efficiency at lower operating frequencies by increasing the electrical size of the patch.

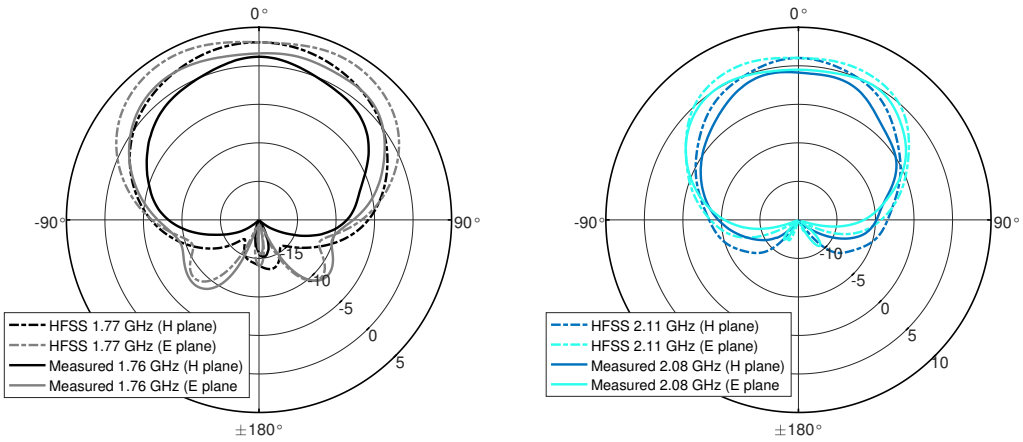

(a) (b)

Figure 5.18: Comparison of realized gain measurements and simulations in the E-plane and H-plane: (a) Realized gain at the lowest tunable frequency, (b) Realized gain at the highest tunable frequency.

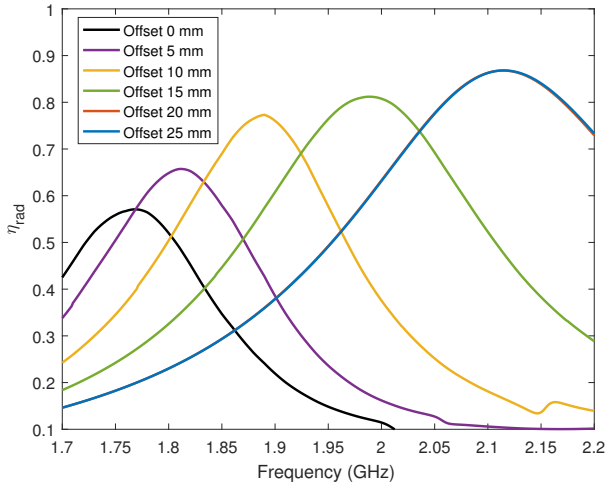

Figure 5.19: Radiation efficiency of the improved patch antenna computed by HFSS.

Asymmetric Tuning

In addition to being tunable in frequency, the patch antenna design has a tunable input impedance. Tuning each stub to a different fluid offset position loads the antenna asymmetrically, and modifies the input impedance of the antenna through movement of the effective electrical location of the feed. In order to test the adaptability of the antenna to environmental effects, two superstrates were applied to the patch antenna at two different configurations.

In the first test case, the antenna was tuned symmetrically to offset values of 10 mm, resulting in an operating frequency of 1.863 GHz. Then, a 60 mil RO3006™ superstrate was taped over the patch, which modified its input impedance and significantly reduced its gain. Finally, the stub closest to the feed was biased to an offset of 17.5 mm, and the other stub was biased to an offset of 12.5 mm. This re-tuned the antenna back to its original operating frequency and input impedance, resulting in a gain pattern nearly identical to the original, as illustrated by Figure 5.20(a). In the second test case, the antenna was tuned originally to an operating frequency of 1.77 GHz. Then, a 120 mil RO3006™ superstrate was loaded onto the antenna to simulate a greater environmental loading effect than in the first case. The additional loading was then compensated for by tuning the stub closest to the feed to an offset of 20 mm. The results for the second test case are depicted in Figure 5.20(b).

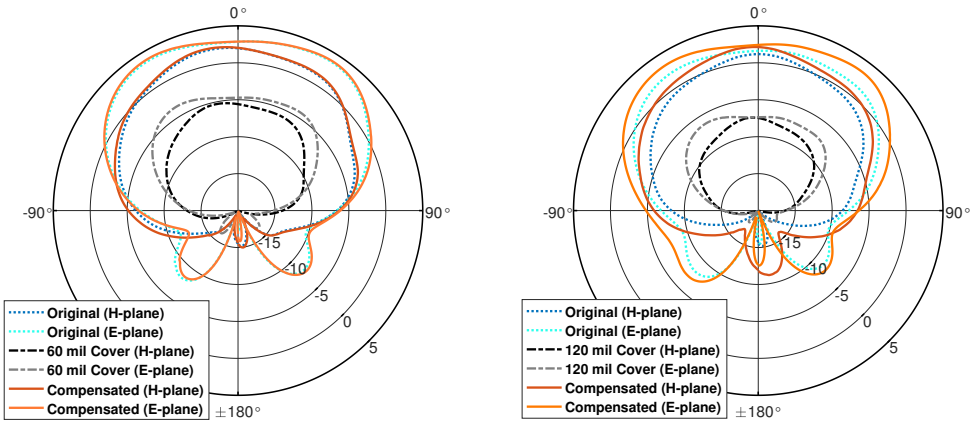

(a) (b)

Figure 5.20: Compensation for loading effects of a RO3006™ superstrate: (a) 60 mil, (b) 120 mil. The superstrate reduces the realized gain (dotted traces), and compensation through asymmetric tuning returns to pattern to the original shape and intensity, shown by the solid traces.

Investigation of Channel Coating

The realized gain measurements of both versions of the single stub patch antenna were consistently 1.5 to 2 dB lower than simulated (Figures 5.6 and 5.18). Part of this discrepancy can be attributed to measurement and calibration error, but another possible explanation is that a thin coating of unbiased or partially biased ferrofluid remains in place inside the channels and is not moved by the bias magnet. Additionally, RO4350B™ is slightly absorbent, so the substrate may absorb a thin layer of ferrofluid as well.

Simulations were run in HFSS with ferrofluid both as a thin inside layer on the channel wall, and as a thin layer absorbed into the substrate. Each layer was assigned different properties depending on its location relative to the bias field and the channel wall. The thin layer labeled “No Bias” inside the channel wall (Figure 5.21) was assigned the properties of EFH1 under zero bias, since this layer was not directly above the bias field in both cases. The “No Bias” layer has a total thickness

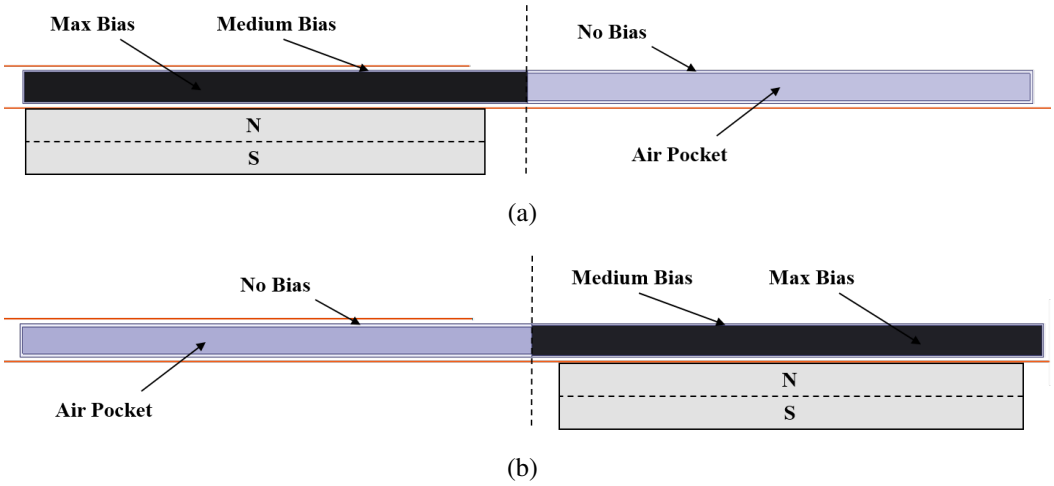

Figure 5.21: Cross-sectional schematic of channel coating simulations: (a) Low frequency configuration, (b) High frequency configuration.

of 6 mils, where the outer half of the layer intersects with the substrate in order to approximate absorption, and the inner half inside of the channel approximates ferrofluid that the bias magnet is unable to move. Fluid absorbed into the substrate likely behaves differently than the bulk of the fluid, so even though the 3 mil layer labeled "Medium Bias" (Figure 5.21) is positioned directly above the bias magnet in both configurations, it is assigned the properties of ferrofluid under a 50 kA/m bias field rather than under the maximum bias field. The ferrofluid block labeled "Max Bias" (Figure 5.21) is assigned the properties of EFH1 under maximum bias, and has the same dimensions as in the original simulations.

As Figure 5.22 shows, addition of layers of unbiased ferrofluid reduces the simulated realized gain to values closer to what was measured. Additionally, the simulated radiation efficiency is reduced by around 30% at the low end of the tunable range, and around 15% at the high end (Figure 5.23). The simulated results support the conclusion that unbiased layers of ferrofluid in the channel have a significant effect on the efficiency of the antenna, and future fabrication should include a PDMS [53] coating of the channel surface to improve fluid biasing and mobility.

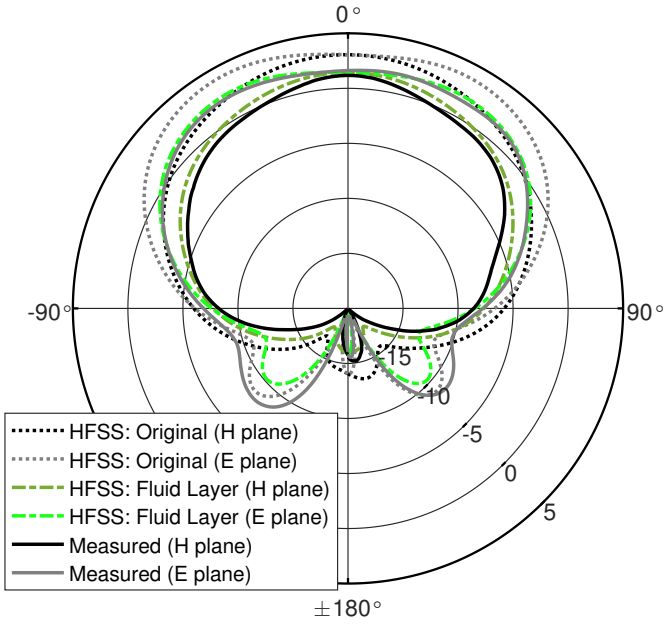

(a)

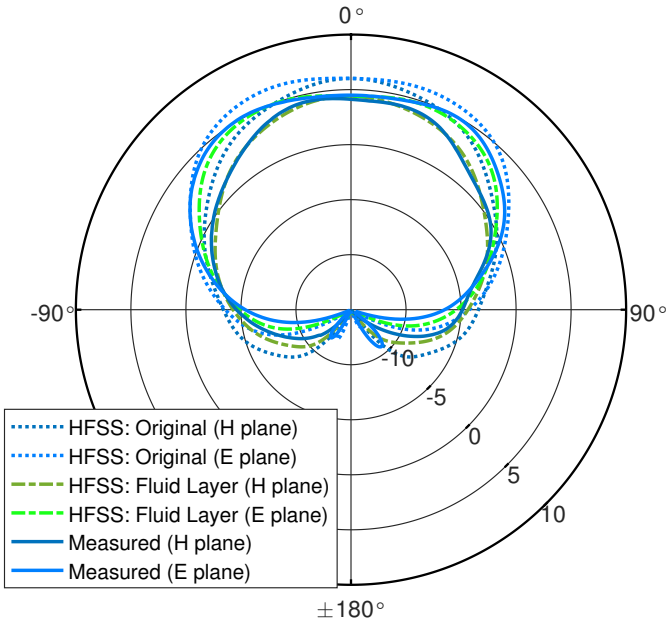

(b)

Figure 5.22: Comparison of realized gain measurements and simulations with and without unbiased fluid layer in the E-plane and H-plane: (a) Realized gain at the lowest tunable frequency, (b) Realized gain at the highest tunable frequency.

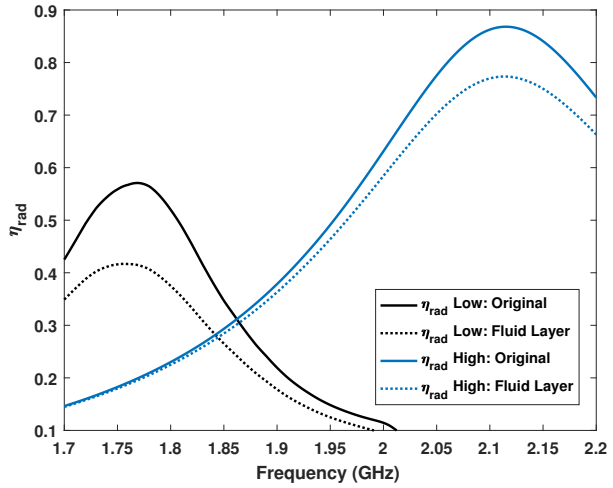

Figure 5.23: Radiation efficiency of the improved patch antenna computed by HFSS with and without unbiased fluid layer.

5.5 Conclusions

Three patch antenna designs using ferrofluid tuning with loaded stubs were presented. The stubs function as tunable reactive loads at the patch edge, improving the efficiency of the antenna over traditional magnetically-tuned antennas loaded with ferrite material in the main substrate of the radiating element. Additionally, as the fluid moves out from beneath the stub, the efficiency increases because the microstrip fields are less exposed to the ferrofluid. This will be improved in future designs with addition of a channel coating, which will improve mobility of the fluid. The improved patch antenna design loaded with a single stub and reduced channel widths has the best combination of tunable fractional bandwidth, efficiency, and reliability out of the three tested patch designs. This is largely due to the single stub requiring less fluid volume, making biasing a simpler process compared to the three stub antenna. When loaded with three stubs, the patch exhibits a greater tuning range in simulation, but measurements show otherwise, likely due to the dif-

ficulties in biasing the fluid entirely. The three stub patch antenna has the added benefit of larger simulated realized gain values across its tunable range, indicating that it has more potential when strictly considering theoretical performance. However, fabrication is markedly more difficult for the three stub design, and the extra volume of fluid required makes effective biasing more difficult because a stronger and larger bias field is required to move the fluid. Additionally, stronger bias fields have greater potential to interact with each other, limiting the potential for accurate tuning of the stubs across their entire range of bias positions. Loading with a single stub at each end simplifies the fabrication process because much smaller channels and fluid volumes are required to load the antenna, making the design simpler overall from a mechanical standpoint.

Chapter 6

Reconfigurable Slot Antenna Using Repositionable Ferrofluid Loads

6.1 Design

A slot antenna is better suited than a patch antenna for operation around 1 GHz and below because a patch would need to have excessively large dimensions in order to be resonant. At frequencies below 1 GHz, a patch antenna will suffer reduced bandwidth and will also have a lower radiation efficiency than a patch of an equivalent substrate height designed to operate at a higher frequency [5]. However, because the fields are oriented differently in a slot antenna, its radiation efficiency is less dependent on its substrate height. In order to avoid complications with fabrication, the substrate height and material are kept the same as with the patch antenna. Due to time constraints and the lack of an accurate transmission line model for the slot antenna, fabrication was not attempted and parametric simulations were run in HFSS as a proof of concept. The work in this chapter shows that the ferrofluid-loaded stub can be used as a reactive load for many radiators – not just patch antennas. The slot antenna has a width of 4 mm and a length of 140 mm. The coupled microstrips have the effect of reducing the slot's resonant frequency, bringing down the second resonance to a usable range closer to 1 GHz.

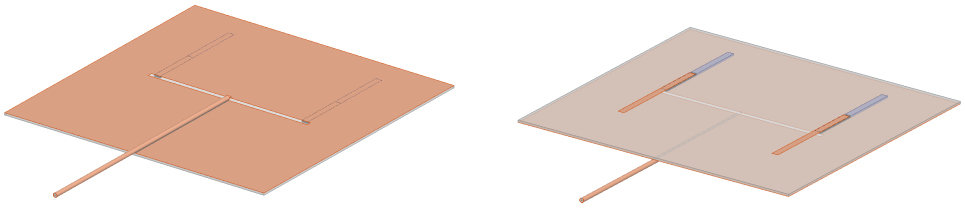

(a) (b)

Figure 6.1: Tunable slot antenna loaded with coupled microstrip lines and fed with a coaxial cable configured as a "Dyson-like" balun [27]: (a) Top view, (b) Bottom view.

The tunable stub-loaded slot antenna relies on coupling between the microstrip stubs and the slot. As seen in Figures 6.1(a) and 6.1(b), the tunable microstrip stubs lie beneath the slot on the other side of the substrate. Ferrofluid between the microstrip lines and the ground plane loads the slot antenna. The microstrip lines are identical, and each has a length of 95 mm, a width of 5 mm, and is offset from the center of the slot by 65 mm. The slot and microstrip line dimensions were chosen through a parametric analysis of the antenna. The slot antenna is fed with a coaxial cable with the outer jacket soldered to the ground plane and the inner conductor extending across the center of the slot and attached to the other side, in a "Dyson-like" balun configuration [27]. This is a somewhat arbitrary feed choice; the slot could also be fed with a coupled microstrip fed across its center, or a coplanar waveguide. Future work will examine the effects of different feeds.

6.2 Transmission Line Model

Analysis of the tunable slot antenna is not as straightforward as with the patch antenna. The slot antenna is modeled following Ruyle's transmission line model for a slot antenna, which can be used to accurately find the input impedance to a center-fed rectangular slot [65]. Ruyle's model is modified by the addition of

load impedances Z_{in1} and Z_{in2} placed at distance l_c from the load impedance Z_L, which accounts for loading effect of the slot ends [65]. Z_{in1} and Z_{in2} represent the input impedance to the coupled microstrip lines seen through Das's ideal coupling transformer [66], and are determined as follows: The input impedance to the ferrofluid-loaded section, Z_{inF} (Figure 6.3), is calculated with the same analysis process detailed in Section 4.2. The contribution from Z_{inM} is given by Pozar [3] as

$$Z_{inM} = -Z_m \coth(\gamma_m(l_{strip} + l_{ocm})) \tag{6.1}$$

where l_{ocm} is determined using [58] with the permittivity of the microstrip with a homogeneous RO4350B™ substrate ($\epsilon_r = 3.48$). Z_{inM} is kept small by choosing $l_{strip} = \frac{\lambda}{4}$ at the center frequency, which also improves the accuracy of the coupling model [66]. Series addition of Z_{inM} and Z_{inF} yields the total input impedance to the microstrip Z_{inT} seen from the microstrip line side of the coupling transformer. Using the ratio

$$Z_{in} = \frac{Z_{inT}}{n^2}, \tag{6.2}$$

the value for Z_{in} seen at the slot side of the coupling transformer is obtained [66].

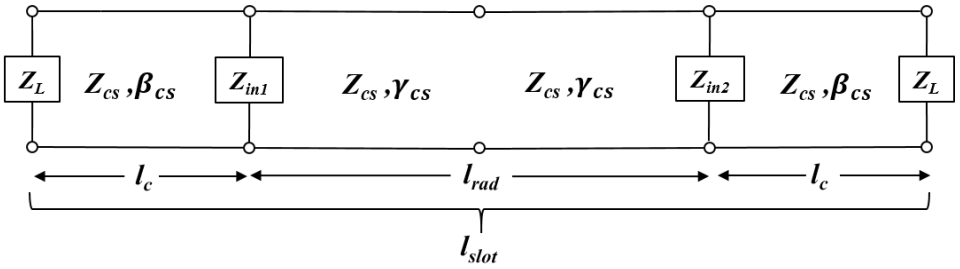

Figure 6.2: Slot antenna transmission line model based on Ruyle's model [65]. Ferrofluid-tunable microstrips are coupled to the slot at distance l_c from the slot end. Input impedances Z_{in1} and Z_{in2} represent the input impedance to the microstrip seen through Das's ideal coupling transformer [66].

The final step in the analysis process is to use Ruyle's transmission line model to

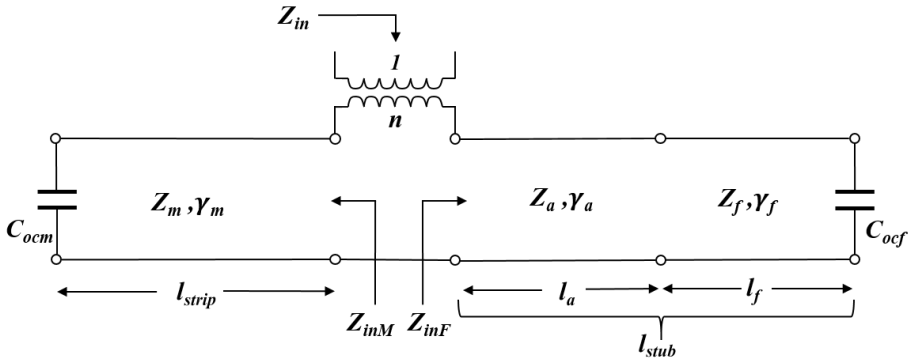

Figure 6.3: Model of the coupled tunable microstrip. The left side is set to $\frac{\lambda}{4}$ at the middle frequency of the tunable range, and the right side is the familiar tunable stub element with l_{stub} set to 40 mm.

determine the input impedance to the center-fed slot. This is done with an "equivalent" slot antenna of length l_{rad} and characteristic impedance and propagation constant Z_{cs} and γ_{cs} respectively, end-loaded with the parallel combination of Z_{LatC} and Z_{in} shown in Figure 6.4. According to [3], the input impedance at distance l_c from the slot end due to Z_L (Figure 6.2) can be found as

$$Z_{LatC} = Z_{cs}\frac{Z_L + jZ_{cs}\tan(\beta_{cs}l_c)}{Z_{cs} + jZ_L\tan(\beta_{cs}l_c)}. \tag{6.3}$$

where Z_{cs} is the characteristic impedance of the slot, and

$$\beta_{cs} = \frac{2\pi}{\lambda_{cs}} \tag{6.4}$$

is the effective wavenumber in the slot calculated using Cohn's method [28]. Lossless calculation of Z_{LatC} is sufficient because l_c is small relative to the total slot length, and the primary loss mechanism of the antenna is radiation, which is captured through analysis of the slot length l_{rad} where $l_{rad} >> l_c$ and $l_{rad} \approx l_{slot}$. Current methods for analyzing the microstrip-to-slot coupling treat the transition as

an ideal transformer with turns ratio $1 : n$ [66]–[68], where n is dependent on the ratio of the slot characteristic impedance and the microstrip characteristic impedance [66]. This analysis typically requires that the lengths of the lines extend past each other by $\frac{\lambda}{4}$ [66]–[68]. This is not practical in the case of the model used here for the antenna, since the distance l_c is less than $\frac{\lambda}{4}$ (Figure 6.2). Minimization of l_c is desirable in order to retain the accuracy of the model, because the slot's radiation conductance is computed for the middle section of the slot between the microstrip coupling points [65] with the assumption that any contribution to radiation from the slot ends is small as long as l_c is kept small relative the total slot length l_{slot}.

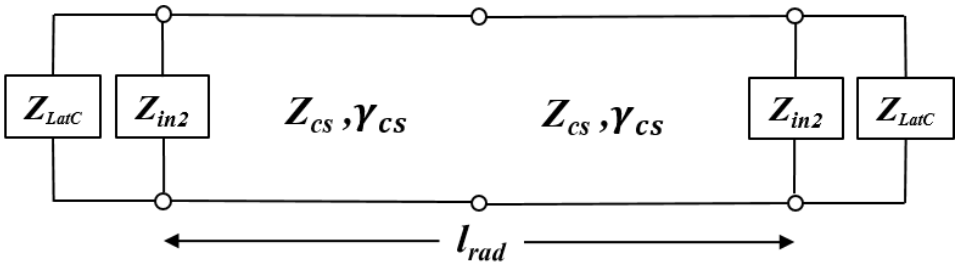

Figure 6.4: Model of the equivalent slot antenna analyzed with Ruyle's model [65].

6.3 Results

The slot antenna has a simulated fractional bandwidth of 10.8% (Figure 6.5(a)). At the ends of the tunable range, the predicted return loss according to the transmission line model does not match with the simulated results (Figure 6.5(b)). The transmission line model does not predict a match at or near the simulated frequencies, though it does predict a single resonance at a lower frequency (Figure 6.6).

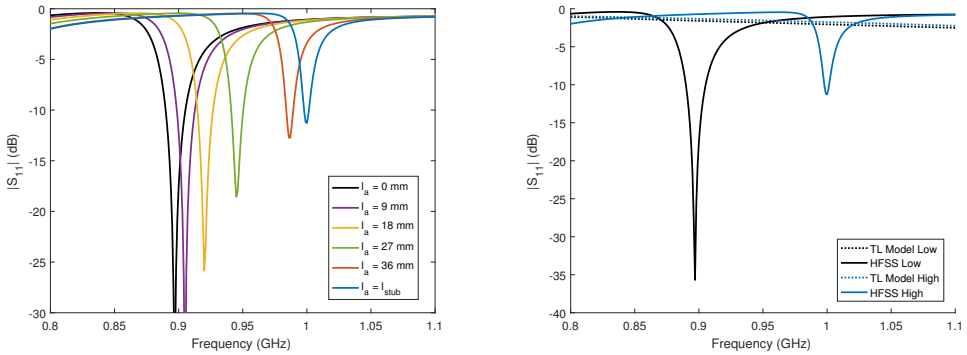

(a) (b)

Figure 6.5: Slot antenna return loss at various bias magnet offset placements as the stubs are tuned symmetrically: (a) Simulated return loss at several offsets, (b) Comparison of calculated and simulated return loss of the slot antenna at the end points of the tunable range. The slot antenna design has a simulated fractional bandwidth of 10.8%, but the transmission line model does not predict any resonances in the same frequency range.

The disagreement between the transmission line model and HFSS is likely due to a higher-order effect for which the model does not account. Inaccuracies in the transmission model are most likely due to the simplistic coupling model, since the microstrips are coupled near the slot ends and the slot does not extend $\frac{\lambda}{4}$ beyond the coupling point. The length l_c from the coupling point to the end of the slot is only 5 mm, which is significantly less than a quarter wavelength in the range of operating frequencies. The accuracy of the coupling model would be improved with an increase in l_c, but the accuracy of the overall transmission line model also depends on the assumption that $l_c << l_{rad}$, as shown in Section 6.2.

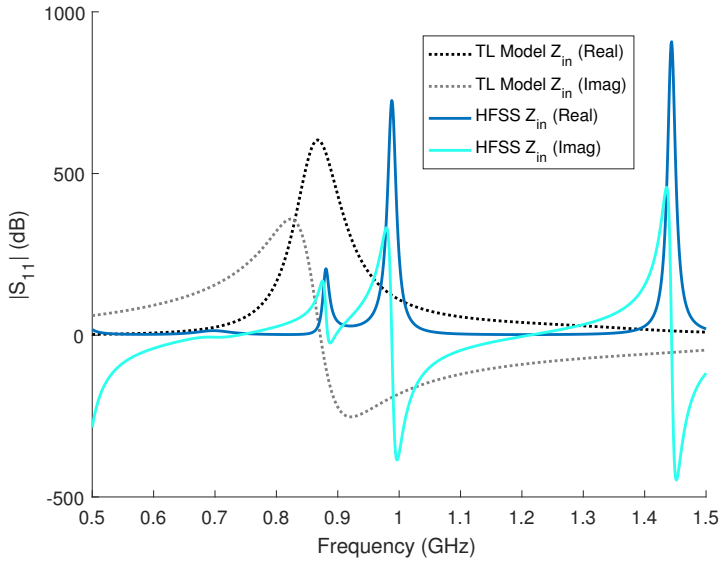

Figure 6.6: Modeled and simulated input impedance to the slot antenna at the lowest tunable frequency where $l_a = 0$ mm. The transmission line model shows a frequency shift from simulation, and also predicts fewer resonances than HFSS in the simulated frequency range.

6.4 Conclusions

As an alternative to the patch antenna, a rectangular slot antenna design was also developed, but not fabricated due to time constraints and lack of an accurate transmission line model. A slot antenna is better suited to operation below 1 GHz because the required size of a patch antenna becomes impractically large at those frequencies. Optimization of the slot antenna design is an ongoing process, as the coupling model characterizing the interaction between the microstrips and the slot is imperfect and limited. However, large scale parametric simulations in HFSS can be run in order to converge on parameters that work optimally for the desired frequency range. The rectangular slot antenna design is a potential solution for applications where a lower frequency range of operation and a less directive pattern is desired.

Chapter 7

Conclusions and Future Work

7.1 Conclusions

As the spectrum continues to fill, tunability is becoming an ever more important trait in RF system design. This work shows that magnetic tuning with ferrofluid can offer strategic design advantages for applications where high electrical isolation and low power consumption is desired. Magnetic tuning is conventionally accomplished through stationary biasing of ferrites, which requires either a controlled current source, or physical access to the device in order to allow for continuous tuning across frequency. The method shown in this work is a novel way to accomplish magnetic tuning, and is more repeatable than conventional microfluidic systems utilizing conductive liquid. The new version of magnetic tuning presented in this work has many advantages over traditional magnetic tuning, such as the ability to continuously tune across frequency with a permanent magnet, and the ability to tune at a distance. The tunable stub can be utilized on its own as a two port microstrip filter element, and can also be loaded onto radiating structures such as patch and slot antennas. End-loading these antennas enables tunability in both operating frequency and input impedance, and the antenna's input impedance can be reconfigured "in situ" to compensate for the loading effect of enclosures through asymmetric tuning

at a distance with an external magnetic field. Ferrofluid actuation is a powerful way to improve the adaptability of microwave devices where low power consumption is desired and physical access to the device is limited.

7.2 Scientific Impact

The tuning method developed as part of this work has several key impacts on the field of microwave engineering. To the best of the author's knowledge, this is the first use of ferrofluid as a movable load beneath a microstrip stub where the primary loading mechanism of the fluid is dielectric. Because the fluid remains under the same magnetic bias intensity regardless of placement, analysis of the fluid's magnetic effects is simplified.

- The loading method shown in this work ensures that the ferrofluid remains under a strong, constant bias field, so its magnetic response and any associated nonlinearities are greatly reduced.
  - Ferrofluid's magnetic properties are used to reposition the fluid, but the loading effect on the overall structure is only weakly magnetic in nature and is primarily dielectric, in contrast to typical designs using ferrofluid.
  - This tuning method has advantages over conventional magnetic loading at UHF because ferromagnetic materials are typically too lossy at these frequencies to function well as tunable loads.
- This work presents a method of magnetic reconfiguration that allows for continuous tuning across frequency with permanent magnets.
  - The nonlinear magnetic response of ferrites is useful for stationary tuning applications, but in order to continuously tune over a frequency

range, an electromagnet is required to generate a continuously adjustable magnetic field.

  - In contrast to solid ferrite materials, ferrofluids are uniquely suited to physical relocation, which allows for continuous tuning through repositioning of the bias field parallel, rather than normal, to the ground plane.
  - The magnetic tuning method presented in this work can be accomplished with permanent magnets, and does not require spacers or physical access to modify the distance between the magnet and the device.

- The antenna designs proposed in this work offer a way to reconfigure both in operating frequency and input impedance.
  - Symmetric tuning of the loading microstrip stubs tunes the operating frequency of the antenna
  - Environmental effects on the antenna's input impedance can be ameliorated with asymmetric tuning of the loads.

7.3 Future Work

Several opportunities for future research exist. The block model (Section 4.2) of the ferrofluid used in simulation and in transmission line modeling is generally an accurate characterization of the fluid placement. Accuracy is reduced for certain channel designs, most notably for channels requiring a large amount of fluid such as the patch antenna loaded with multiple stubs demonstrated in Section 5.3. Work remains in optimization of the channel shape and size such that an appropriate volume of fluid is used. In addition, coating the channel with PDMS [53] or a similar compound will improve the accuracy of the model, as the fluid will leave less

residue on the channel surface. A coating will likely reduce loss due to the fluid by improving fluid mobility and ensuring that more of the fluid is biased as expected. These design improvements come at the cost of increased fabrication complexity; however, 3D printing technology has advanced to the point where multiple materials can be printed on a single printer, enabling 3D printing of antennas [50]. As this technology continues to progress, improved designs using ferrofluid-based tuning will become more practical. An advantage of the additive manufacturing process is that channels can be formed as part of the substrate, increasing the variety of available channel shapes and sizes. 3D printing of substrates will also simplify the addition of an oloephobic coating to the channel, and will facilitate reduction or even complete removal of the sandwich layers necessary in the current design, resulting in a larger range of tunable reactances for the stub. Removal of substrate sandwich layers will also improve the loading effect of the ferrofluid on the overall capacitance of the channel, because even thin sandwich layers of substrate with a lower permittivity than the load can result in a large reduction of the capacitance of the overall substrate [52]. Future research should include testing of other varieties of ferrofluids, and a study of the longevity of ferrofluid-tunable devices operating under a constant bias field, as ferrofluid has the tendency to agglomerate over time when exposed to a permanent magnetic bias field greater than 100 mT [69].

Opportunities for future research on antenna loading also exist. As shown by the reduction in measured realized gain of the patch antenna designs compared to simulation, loss due to unbiased ferrofluid can reduce the efficiency of the antenna. Thus, minimization of the volume of fluid is desirable in order to increase the likelihood that the fluid is completely biased, and that loss remains low. Fluid volume can be reduced by decreasing the channel width, as shown by the improved patch antenna in Section 5.4. However, channel width has an effect on the tunable range

of the antenna, which is dependent, in part, on the filling fraction of the microstrip fields [64]. The filling fraction is ultimately depending on the dimensions of the loading stub, which are determined in this work through an optimization procedure in MATLAB® utilizing the patch antenna transmission line model (Section 5.1). In its current form, the transmission line model exhibits a slight frequency shift from the measured and simulated results across the entire tunable range. Further work should be done to better capture the loading behavior of the tunable stubs in order to improve the accuracy of the patch antenna transmission line model and optimization process. From there, decisions about the channel size and shape will depend on the filling fraction of the fields, and the desired trade-off between tuning range and antenna efficiency. The slot antenna design was developed through a parametric analysis in HFSS, as the coupling mechanism between the loaded microstrips and the slot is not currently well-characterized by the ideal transformer model proposed by [66] because the microstrips are significantly less than a quarter wavelength from the ends of the slot. As shown by [68], a simple turns ratio is not sufficient to fully capture the coupling behavior between the microstrip and slot. Thus, future research remains to better characterize the coupling behavior. As with the patch antenna, improvements to the transmission line model will facilitate design guidelines for the slot antenna ferrofluid channel design as well, enabling exciting opportunities for future tunable antenna designs utilizing ferrofluid loads.

References

[1] K. B. Letaief and W. Zhang, "Cooperative communications for cognitive radio networks", *Proceedings of the IEEE*, vol. 97, no. 5, pp. 878–893, 2009.

[2] J. T. Bernhard, "Reconfigurable antennas", *Synthesis lectures on antennas*, vol. 2, no. 1, pp. 1–66, 2007.

[3] D. M. Pozar, *Microwave Engineering*. Wiley & Sons, 2012, vol. 4.

[4] J. T. Aberle, S.-H. Oh, D. T. Auckland, and S. D. Rogers, "Reconfigurable antennas for wireless devices", *IEEE Antennas and Propagation Magazine*, vol. 45, no. 6, pp. 148–154, 2003.

[5] C. A. Balanis, *Antenna theory: Analysis and design*. John Wiley & Sons, 2016.

[6] P. Bhartia and I. Bahl, "A frequency agile microstrip antenna", in *Antennas and Propagation Society International Symposium, 1982*, IEEE, vol. 20, 1982, pp. 304–307.

[7] P. Haskins, P. Hall, and J. Dahele, "Active patch antenna element with diode tuning", *Electronics Letters*, vol. 27, no. 20, pp. 1846–1848, 1991.

[8] P.-Y. Qin, Y. J. Guo, Y. Cai, E. Dutkiewicz, and C.-H. Liang, "A reconfigurable antenna with frequency and polarization agility", *IEEE Antennas and Wireless Propagation Letters*, vol. 10, pp. 1373–1376, 2011.

[9] N. Nguyen-Trong, L. Hall, and C. Fumeaux, "A frequency-and polarization-reconfigurable stub-loaded microstrip patch antenna", *IEEE Transactions on Antennas and Propagation*, vol. 63, no. 11, pp. 5235–5240, 2015.

[10] D. Pozar and V. Sanchez, "Magnetic tuning of a microstrip antenna on a ferrite substrate", *Electronics Letters*, vol. 24, no. 12, pp. 729–731, 1988.

[11] P. Rainville and F. Harackiewicz, "Magnetic tuning of a microstrip patch antenna fabricated on a ferrite film", *Articles*, p. 5, 1992.

[12] L.-R. Tan, R.-X. Wu, C.-Y. Wang, and Y. Poo, "Magnetically tunable ferrite loaded SIW antenna", *IEEE Antennas and Wireless Propagation Letters*, vol. 12, pp. 273–275, 2013.

[13] J. Kiriazi, H. Ghali, H. Ragaie, and H. Haddara, "Reconfigurable dual-band dipole antenna on silicon using series MEMS switches", in *Antennas and Propagation Society International Symposium, 2003. IEEE*, IEEE, vol. 1, 2003, pp. 403–406.

[14] A. G. Besoli and F. De Flaviis, "A multifunctional reconfigurable pixeled antenna using mems technology on printed circuit board", *IEEE Transactions on Antennas and Propagation*, vol. 59, no. 12, pp. 4413–4424, 2011.

[15] G. J. Hayes, J.-H. So, A. Qusba, M. D. Dickey, and G. Lazzi, "Flexible liquid metal alloy (egain) microstrip patch antenna", *IEEE transactions on Antennas and Propagation*, vol. 60, no. 5, pp. 2151–2156, 2012.

[16] M. R. Khan, G. J. Hayes, S. Zhang, M. D. Dickey, and G. Lazzi, "A pressure responsive fluidic microstrip open stub resonator using a liquid metal alloy", *IEEE Microwave and Wireless Components Letters*, vol. 22, no. 11, pp. 577–579, 2012.

[17] C. Koo, B. E. LeBlanc, M. Kelley, H. E. Fitzgerald, G. H. Huff, and A. Han, "Manipulating liquid metal droplets in microfluidic channels with minimized skin residues toward tunable RF applications", *Journal of Microelectromechanical Systems*, vol. 24, no. 4, pp. 1069–1076, 2015.

[18] T. Palomo and G. Mumcu, "Microfluidically reconfigurable metallized plate loaded frequency-agile RF bandpass filters", *IEEE Transactions on Microwave Theory and Techniques*, vol. 64, no. 1, pp. 158–165, 2016.

[19] E. Andreou, T. Zervos, F. Lazarakis, A. Alexandridis, K. Dangakis, E. Varouti, G. Fikioris, and J. Vardaxoglou, "Reconfigurable proximity coupled patch antenna using magnetic bias", in *Antennas and Propagation Conference (LAPC), 2014 Loughborough*, IEEE, 2014, pp. 376–380.

[20] C. Wu, Y. Zhang, and Q. Liu, "A magnetically controlled reconfigurable antenna using a reed switch", in *Signal Processing, Communication and*

Computing (ICSPCC), 2013 IEEE International Conference on, IEEE, 2013, pp. 1–4.

[21] J.-C. Langer, J. Zou, C. Liu, and J. T. Bernhard, "Micromachined reconfigurable out-of-plane microstrip patch antenna using plastic deformation magnetic actuation", *IEEE Microwave and Wireless Components Letters*, vol. 13, no. 3, pp. 120–122, 2003.

[22] T. Tsutaoka, T. Kasagi, and K. Hatakeyama, "Permeability spectra of yttrium iron garnet and its granular composite materials under DC magnetic field", *Journal of Applied Physics*, vol. 110, no. 5, p. 053 909, 2011.

[23] A. Goldman, *Modern ferrite technology*. Springer Science & Business Media, 2006.

[24] D. K. Cheng *et al.*, *Field and wave electromagnetics*. Pearson Education India, 1989.

[25] *Part 5: Magnetic materials — itaca*, http://www.itacanet.org/basic-electrical-engineering/part-5-magnetic-materials/, (accessed April 11th, 2017).

[26] *Emi absorbers — kitagawa industries america, inc. - emi/rfi shielding components.* http://kgs-ind.com/products/emc/emi-absorbers/, (accessed April 11th, 2017).

[27] J. Dyson, "The equiangular spiral antenna", *IRE Transactions on Antennas and Propagation*, vol. 7, no. 2, pp. 181–187, 1959.

[28] S. B. Cohn, "Slot line on a dielectric substrate", *Microwave Theory and Techniques, IEEE Transactions on*, vol. 17, no. 10, pp. 768–778, 1969.

[29] S. Cohn, "Sandwich slot line (correspondence)", *Microwave Theory and Techniques, IEEE Transactions on*, vol. 19, no. 9, pp. 773–774, 1971.

[30] A. Nicolson and G. Ross, "Measurement of the intrinsic properties of materials by time-domain techniques", *Instrumentation and Measurement, IEEE Transactions on*, vol. 19, no. 4, pp. 377–382, 1970.

[31] W. B. Weir, "Automatic measurement of complex dielectric constant and permeability at microwave frequencies", *Proceedings of the IEEE*, vol. 62, no. 1, pp. 33–36, 1974.

[32] S. Papell, “Magnetic fluid readily controlled in zero gravity environment”, 1965.

[33] P. Fannin, “Characterisation of magnetic fluids”, *Journal of alloys and compounds*, vol. 369, no. 1, pp. 43–51, 2004.

[34] *Emg water-based series - ferrofluids*, https://ferrofluid.ferrotec.com/products/ferrofluid/emg/water/, 2017 (accessed April 11th, 2017).

[35] B. Assadsangabi, M. S. M. Ali, and K. Takahata, “Planar variable inductor controlled by ferrofluid actuation”, *IEEE Transactions on Magnetics*, vol. 49, no. 4, pp. 1402–1406, 2013.

[36] J. Yao, S. Liu, Z. Li, and D. Li, “A novel ferrofluid inclinometer exploiting a Hall element”, *IEEE Sensors Journal*, vol. 16, no. 22, pp. 7986–7991, 2016.

[37] W. Lin, B. Liu, H. Zhang, B. Song, D. Yan, Y. Miao, H. Liu, and Y. Liu, “Laser-induced thermal effect for tunable filter employing ferrofluid and fiber taper coupler”, *Photonics Technology Letters, IEEE*, vol. 27, no. 22, pp. 2339–2342, 2015.

[38] L. Néel, “Influence des fluctuations thermiques sur laimantation de grains ferromagnetiques tres fins”, *Comptes Rendus Hebdomadaires Des Seances De L Academie Des Sciences*, vol. 228, no. 8, pp. 664–666, 1949.

[39] W. Coffey and P. Fannin, “Internal and Brownian mode-coupling effects in the theory of magnetic relaxation and ferromagnetic resonance of ferrofluids”, *Journal of Physics: Condensed Matter*, vol. 14, no. 14, p. 3677, 2002.

[40] S. May, “Rotational relaxation dynamics of ferrofluid systems”, *The University of Hull, Thesis submitted for the degree of Master of Science*, pp. 1–110, 2011.

[41] P. Fannin, “Investigating magnetic fluids by means of complex susceptibility measurements”, *Journal of magnetism and magnetic materials*, vol. 258, pp. 446–451, 2003.

[42] G. Bellizzi and O. Bucci, “A novel measurement approach for the broadband characterization of diluted water ferrofluids”, in *Antennas and Propagation (EUCAP), 2012 6th European Conference on*, IEEE, 2012, pp. 3651–3654.

[43] F. Grover, “Inductance calculations: Dover phoenix editions”, 2004.

[44] F. R. Crownfield Jr, "Optimum spacing of coil pairs", *Review of Scientific Instruments*, vol. 35, no. 2, pp. 240–241, 1964.

[45] *Ferrotec — manufacturing advanced material, component, and system solutions for precision processes - corporate*, https://www.ferrotec.com/, 2017 (accessed April 11th, 2017).

[46] *Efh series educational ferrofluid — type: Efh1*, https://ferrofluid.ferrotec.com/products/ferrofluid-educational-fluid/efh/EFH1/, 2017 (accessed April 11th, 2017).

[47] *Emg series - oil-based ferrofluid — type: Emg 900*, https://ferrofluid.ferrotec.com/products/ferrofluid-emg/oil/EMG-900/, 2017 (accessed April 11th, 2017).

[48] *Emg series - water-based ferrofluid — type: Emg 700*, https://ferrofluid.ferrotec.com/products/ferrofluid-emg/water/emg-700/, 2017 (accessed April 11th, 2017).

[49] P. Fannin, A. Giannitsis, and S. Charles, "Frequency-dependent loss tangent and power factor of magnetic fluids", *Journal of magnetism and magnetic materials*, vol. 226, pp. 1887–1889, 2001.

[50] M. Liang, C. Shemelya, E. MacDonald, R. Wicker, and H. Xin, "3-D printed microwave patch antenna via fused deposition method and ultrasonic wire mesh embedding technique", *IEEE Antennas and Wireless Propagation Letters*, vol. 14, pp. 1346–1349, 2015.

[51] A. Horton, S. Chilton, H. Sigmarsson, and J. Ruyle, "Tunable microstrip filter element using magnetically-repositioned ferrofluid load", *Electronics Letters*, 2017.

[52] R. Garg, I. Bahl, and M. Bozzi, *Microstrip lines and slotlines*. Artech house, 2013.

[53] B. J. Basu, V. D. Kumar, and C. Anandan, "Surface studies on superhydrophobic and oleophobic polydimethylsiloxane–silica nanocomposite coating system", *Applied Surface Science*, vol. 261, pp. 807–814, 2012.

[54] N. Hosseini, N. S. Esmaeilzad, and O. A. Civi, "Tunable frequency antenna integrated with microfluidic channel", in *Antennas and Propagation & US-*

NC/URSI National Radio Science Meeting, 2015 IEEE International Symposium on, IEEE, 2015, pp. 2303–2304.

[55] A. Sihvola, "Mixing rules with complex dielectric coefficients", *Subsurface Sensing Technologies and Applications*, vol. 1, no. 4, pp. 393–415, 2000.

[56] E. Hammerstad and O. Jensen, "Accurate models for microstrip computer-aided design", in *Microwave Symposium Digest, 1980 IEEE MTT-S International*, IEEE, 1980, pp. 407–409.

[57] R. A. Pucel and D. J. Massé, "Microstrip propagation on magnetic substrates—part I: Design theory", *IEEE Transactions on Microwave Theory and Techniques*, vol. 20, no. 5, pp. 304–308, 1972.

[58] M. Kirschning, R. Jansen, and N. Koster, "Accurate model for open end effect of microstrip lines", *Electronics Letters*, vol. 3, no. 17, pp. 123–125, 1981.

[59] ANSYS, "Electronics Desktop", *Pittsburgh, PA*, 2015.

[60] S. Davidson, S. Long, and W. Richards, "Dual-band microstrip antennas with monolithic reactive loading", *Electronics Letters*, vol. 21, no. 20, pp. 936–937, 1985.

[61] M. Deshpande and M. Bailey, "Analysis of stub loaded microstrip patch antennas", in *Antennas and Propagation Society International Symposium, 1997. IEEE., 1997 Digest*, IEEE, vol. 2, 1997, pp. 610–613.

[62] A. A. Deshmukh, G. Ankit, C. Harsh, S. Rahil, S. Sneha, and K. Ray, "Analysis of stub loaded circular microstrip antennas", in *Advances in Computing and Communications (ICACC), 2012 International Conference on*, IEEE, 2012, pp. 282–285.

[63] H. Pues and A. Van de Capelle, "Accurate transmission-line model for the rectangular microstrip antenna", in *IEEE Proceedings H (Microwaves, Optics and Antennas)*, IET, vol. 131, 1984, pp. 334–340.

[64] H. A. Wheeler, "Transmission-line properties of parallel strips separated by a dielectric sheet", *IEEE Transactions on Microwave Theory and Techniques*, vol. 13, no. 2, pp. 172–185, 1965.

[65] J. Ruyle and J. Bernhard, "A wideband transmission line model for a slot antenna", *IEEE Transactions on Antennas and Propagation*, vol. 61, no. 3, pp. 1407–1410, 2013.

[66] N. K. Das, "Generalized multiport reciprocity analysis of surface-to-surface transitions between multiple printed transmission lines", *IEEE transactions on microwave theory and techniques*, vol. 41, no. 6, pp. 1164–1177, 1993.

[67] J. B. Knorr, "Slot-line transitions (short papers)", *IEEE transactions on Microwave Theory and Techniques*, vol. 22, no. 5, pp. 548–554, 1974.

[68] A. Matland, "Improved vertical coupling between printed planar transmission lines", Master's thesis, UNIVERSITY OF OKLAHOMA, 2016.

[69] V. Rene, email correspondence, 2017.